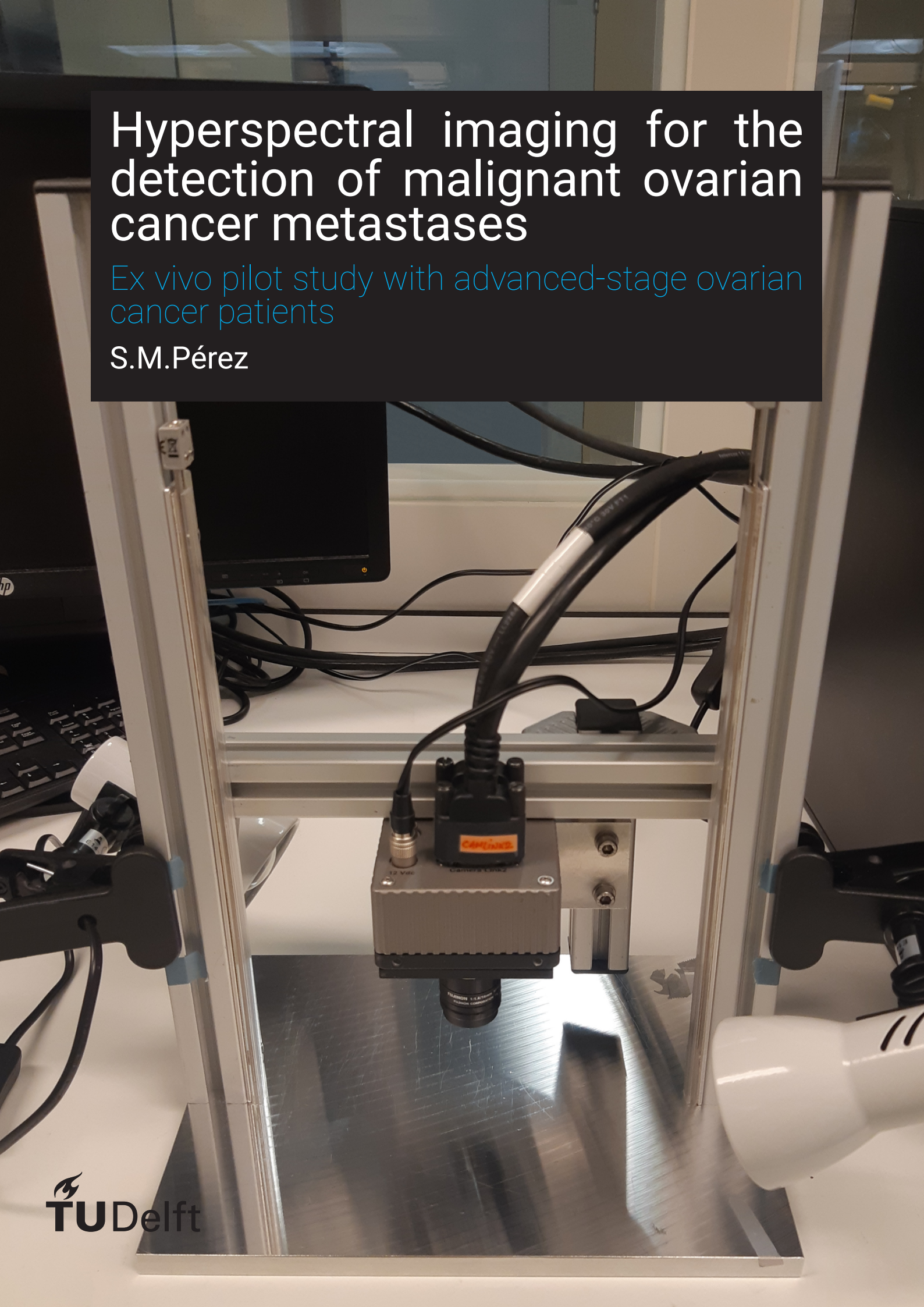

Hyperspectral imaging for the detection of malignant ovarian cancer metastases

Ex vivo pilot study with advanced-stage ovarian cancer patients

S.M.Pérez

TU Delft

Hyperspectral imaging for the detection of malignant ovarian cancer metastases

Ex vivo pilot study with advanced-stage ovarian cancer patients

by

S.M.Pérez

to obtain the degree of Master of Science
at the Delft University of Technology,
to be defended publicly on Monday January 25, 2021 at 3:00 PM.

Student number:	4208277	
Project duration:	February 1, 2020 – Januari 25, 2020	
Thesis committee:	Prof. dr. J. Dankelman,	TU Delft, supervisor
	Prof. dr. B.H.W. Hendriks,	TU Delft, supervisor
	Drs. G.M. Nieuwenhuyzen,	Erasmus MC, supervisor
	Dr. ir. N.J.P. van de Berg,	Erasmus MC, supervisor
	Dr. N. Bhattacharya,	TU Delft, committee member

TU Delft

Erasmus MC
University Medical Center Rotterdam

Preface

S.M.Pérez
Delft, January 2021

I am grateful for all the people who supported me during this thesis project. I enjoyed working on this project together. I would like to thank Gatske Nieuwenhuyzen and Nick van de Berg from the Erasmus MC, Gynaecology department for the support during clinical research and enthusiasm to take this project to the next level. I would like to thank Marco Lai and Francesca Manni, PhD candidates in hyperspectral imaging from Phillips and Eindhoven University of Technology, for all the time, patience and help with the preprocessing of the hyperspectral data and optimisation of the classifier. I would like to thank Patricia Ewing and Lucia Rijstenberg from the Erasmus MC, Pathology department for the great help and lots of time spend in the pathological lab for the resection, imaging and pathological annotation of the tissues. I would like to thank Marianne Maliepaard from the Erasmus MC, Gynaecology department for assistance during patient inclusion. I would like to thank Marta Jozwiak from the Erasmus MC, Gynaecology department for the flying start we made during the first months to get approval to do our research. Furthermore, I would like to thank Nandini Bhattacharya from Delft University of Technology, precision and microsystems engineering department for forming part of the graduation committee. I would like to thank Jenny Dankelman and Benno Hendriks from Delft University of Technology, BioMechanical department and Heleen Beekhuizen from Erasmus MC, Gynaecology department. Without you, this whole project could not exist. You foresaw that joining the technical and medical insights could be a solution to enhance the removal of microscopic malignant ovarian metastasis and increase the progression-free survival of patients with advanced-stage ovarian cancer. Last but not least, I would like to thank all my friends and family for their enthusiasm, support, relaxing moments and interesting questions during this thesis project.

This project was a collaboration between Delft University of technology, BioMedical Engineering department and Erasmus MC, Gynaecology department.

Abstract

BACKGROUND: Ovarian cancer is the number eight cause of cancer-related mortality in women around the world and has an incidence of more than 295 000 and mortality of almost 158 000. The most important prognostic factor for the survival of advanced-stage ovarian cancer is the complete resection of all microscopic tumour tissue during cytoreductive surgery. Still, even after complete CRS and removal of all visible and palpable tumours, more than two-thirds of women with advanced-stage ovarian cancer experience recurrence due to microscopic residual tumour. Therefore, an intraoperative visualisation technique is of great importance to detect these microscopic tumours. In this pilot study, the feasibility of NIR hyperspectral imaging for the detection of malignant ovarian cancer metastases was evaluated ex vivo.

METHOD: Patients with suspected primary ovarian cancer planned for cytoreductive surgery were enrolled in the study. Hyperspectral images from the resected tissue were acquired in the wavelength range of 665-975 nm. All hyperspectral data was preprocessed by image calibration, min-max normalisation and noise filtering. The the most important features were selected before implementing the hyperspectral data in the classifier. The linear SVM, RBF SVM, and a k-NN classifier were used to discriminate malignant ovarian tissue from the surrounding tissue. The performance of the classifier was evaluated by leave-one-out cross-validation.

RESULTS: Ten patients were included in the study. The linear SVM classifiers had the highest performance with a sensitivity of 0.81, a specificity of 0.75, AUC of 0.83 and MCC of 0.41. Thereafter came the RBF SVM classifier followed by the k-NN classifier.

CONCLUSION: This pilot study shows that hyperspectral imaging with the use of a linear SVM classifier is a promising technique to discriminate malignant ovarian tissue from the surrounding tissue. Hyperspectral imaging can scan a whole area, is fast, non-contact, non-invasive and can be used inside the operation room. However, before HSI can be implemented in real practice, further validation is required in vivo and technical enhancements need to be made such as enlarging the training data set, evaluate the SWIR wavelength range, include a registration algorithm which accounts for elastic deformation of the tissue, evaluate several feature selection methods, and compare other classifiers.

Keywords: Hyperspectral imaging, ovarian cancer, classification

Contents

List of Figures

List of Tables

List of abbreviations

AUC: Area under the curve
CMOS: Complementary metal oxide semiconductor
CNN: Convolutional neural network
CRS: Cytoreductive surgery
CT: Computed tomography
DNN: Deep neural network
EPR: Enhanced vascular permeability and retention
FIGO: Federation of Gynaecology and Obstetrics
H&E: Hematoxylin and eosin
HIPEC: Heated intraperitoneal chemotherapy
HS: Hyperspectral
HSI: Hyperspectral imaging
HSV: Hue, saturation, value
ICG: Indocyanine green
ICS: Interval cytoreductive surgery
k-NN: k-Nearest neighbour
LDA: Linear discriminant analysis
MLP: Multilayer perceptron
MMC: Matthews correlation coefficient
MRI: Magnetic resonance imaging
NACT: Neoadjuvant chemotherapy
NIR: Near infra-red
NPV: Negative predicted value
PCA: Principle component analysis
PDS: Primary debulking surgery
PET: Positron emission tomography
PPV: Positive predictive value
QDA: Quadratic discriminant analyse
RBF: Radial based kernel function
RF: Random forest
RGB: Red, green, blue
ROC: Receiver operating characteristic
SERS: Surface-enhanced Raman spectroscopy
SERRS: Surface-enhanced resonance Raman scattering
SVM: Support vector machine
SWIR: Short-wave infrared
VIS: Visible
WHO: World Health Organisation
5-ALA: 5-Aminolevulinic acid

1

Introduction

1.1. Ovarian cancer

Ovarian cancer is the number eight cause of cancer-related mortality in women around the world with an incidence of 295 414 and mortality of 184 799 in 2018 [5]. Prodromal symptoms tend to be vague and can include pain in the abdomen or pelvis, distended non-tender abdomen, constipation, fatigue, weight loss, palpable mass, tachycardia, and deep vein thrombosis [36]. There are many types of ovarian cancer. The World Health Organisation (WHO) classifies ovarian cancer into several different groups according to the tissue of origin. These include surface epithelial ovarian tumours (65%) which develop from cells on the outer surface of the ovary, germ cell ovarian tumours (15%) which develop from cells that produce ova, sex cord-stromal ovarian tumours (10%) which develop from connective tissue inside the ovaries, metastases (5%), and miscellaneous (5%). These groups can be subdivided into cell types and atypia (benign, borderline, malignant)[40] [31][8]. The different types of ovarian cancer according to the tissue of origin can be seen in Figure 1.1.

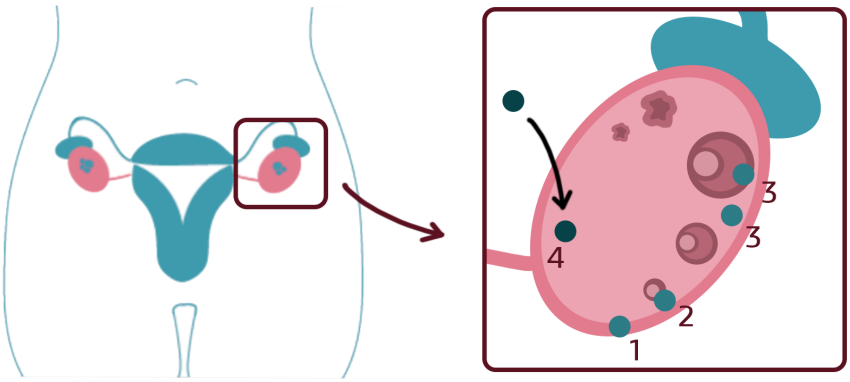

Figure 1.1: The types of ovarian cancer are: 1. Surface epithelial ovarian tumour, which develop from cells on the outer surface of the ovary 2. Germ cell ovarian tumour, which develop from cells that produce ova 3. Sex cord-stromal ovarian tumour, which develop from connective tissue inside the ovaries 4. metastases 5. Miscellaneous, with each their own cell types (adapted from [16])

Ovarian cancer is staged using the International Federation of Gynaecology and Obstetrics (FIGO) staging system. The stages of ovarian cancer are based on the extension of the tumour, the spread to the lymph nodes and the spread to distant sites. At FIGO stage I, the tumour is confined to ovaries or fallopian tubes. At FIGO stage II the tumour involves one or both ovaries or fallopian tubes with pelvic extension below the pelvic brim or primary peritoneal cancer. At FIGO stage III, the tumour involves one or both ovaries or fallopian tubes, or primary peritoneal cancer, with spread to the peritoneum outside the pelvis and/or metastasis to the retroperitoneal lymph nodes. And at FIGO stage IV the tumour includes distant metastasis in the liver, spleen, intestines, lungs or other tissue [31]. The FIGO stages of ovarian cancer can be seen in Figure 1.2. The ovarian cancer cells are graded by comparing the tumour cells with healthy cells and is based on the combined scores

for architecture nuclear atypia, and mitotic activity. Low-grade (grade 1) or well-differentiated tumour cells look similar to normal cells, usually grow slowly and are less likely to spread. Intermediate-grade (grade 2) or moderately differentiated tumour cells look more abnormal and are slightly-fast growing, high-grade (grade 3) or poorly differentiated cancer cells look very different from normal cells and may grow more quickly [16]. Due to the difficult presentation of ovarian cancer, 75% of women are diagnosed at an advanced stage (FIGO IIIB - IV) [50]. The approximate 5-year survival rate is dependent on the stage of ovarian cancer. The 5-year survival rate of stage I is 90%, stage II is 65%, stage III is 40% and stage IV is 18% [1].

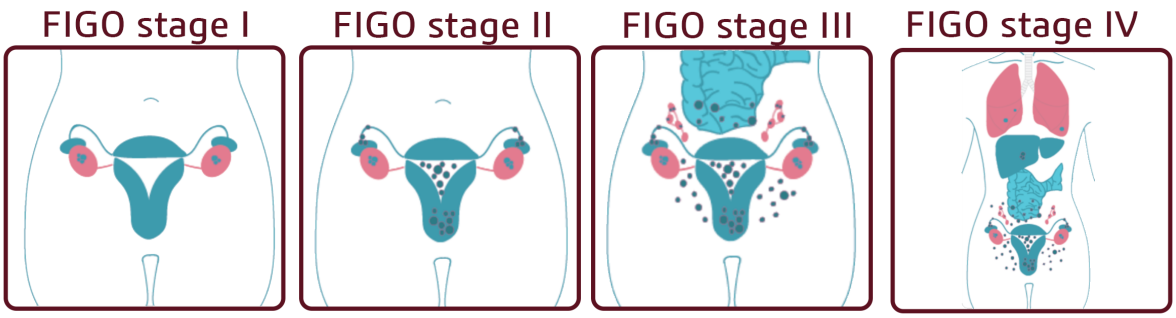

Figure 1.2: Stages of ovarian cancer are: I Ovaries or fallopian tubes II one or both ovaries or fallopian tubes with a pelvic extension below the pelvic brim or primary peritoneal cancer III One or both ovaries or fallopian tubes, or primary peritoneal cancer, with spread to the peritoneum outside the pelvis and/or metastasis to the retroperitoneal lymph nodes IV Distant metastasis (adapted from [16])

1.2. Treatment of ovarian cancer

When ovarian cancer is suspected, primary evaluation consists of physical examination, imaging of the abdomen, pelvis, and chest with computed tomography (CT), magnetic resonance imaging (MRI) or positron emission tomography (PET) and laparotomy or laparoscopy with biopsy to evaluate the extent of the disease, determine the feasibility of surgical resection and confirm the diagnosis [50]. When early-stage ovarian cancer is detected, laparotomic or laparoscopic comprehensive surgical staging is recommended. Dependent on the presence of complete surgical staging and the stage of the disease, adjuvant chemotherapy treatment is recommended. The comprehensive surgical staging usually includes peritoneal washings, removal of the uterus (hysterectomy), both ovaries (bilateral salpingo-oophorectomy), omentum (omentectomy) and pelvic and para-aortic lymph nodes. Furthermore, the peritoneal surfaces of the diaphragm, paracolic gutters, and pelvis are examined or sampled. In some cases conservative sparing surgery is possible. A common intervention for advanced staged ovarian cancer is a comprehensive surgical debulking with maximal cytoreductive surgery (CRS) of all visible tumours and chemotherapy [36]. During CRS, the whole peritoneal cavity is exposed and all tumours are inspected and palpated. Thereafter, all tumour tissue is removed. If the tumours are extended to the splenic hilum, the omentum and spleen, they are resected together en bloc. Tumours in the pelvis, including tumour at the uterus, ovaries, and rectum, are resected en bloc. Tumours at the small bowel, colon, and paracolic gutter are resected individually or together with other surgical procedures [24]. Primary debulking surgery (PDS) before initiation of chemotherapy can be done. In the case of FIGO stage III disease and cytoreductive surgery until lesions <2,5 mm also heated intraperitoneal chemotherapy (HIPEC) during surgery can be given. In case of a low likelihood to achieve complete cytoreductive surgery or in case of FIGO stage IV disease, neoadjuvant chemotherapy (NACT) followed by interval cytoreductive surgery (ICS) is recommended [50].

1.3. Problem definition

Complete resection of all macroscopic disease is the strongest independent variable in predicting overall survival [24]. However, even after complete CRS and removal of all visible and palpable tumours, more than two-thirds of the women with advanced epithelial ovarian cancer experience recurrence. Microscopic residual tumour seems to be the source of peritoneal recurrence. If microscopic, invisible and non-palpable tumour could be detected by an intraoperative imaging technique and resected completely during surgery, the progression-free survival can be increased [24]. Furthermore, when no microscopic tumour is detected, resection is not necessary. As a result, the duration of surgery and recovery can be shortened, and the patient

can (re) start chemotherapy earlier.

There are currently several intraoperative visualisation techniques in use or development for the detection of ovarian cancer metastasis. Cryosection is a widely used intraoperative diagnostic technique where a small piece of the suspicious tissue is sent to the pathology lab where the tissue is frozen with Cryostat, sliced in sections of 7 to 8 μm, stained with hematoxylin, eosin and toluidine blue, and microscopically examined by the pathologist. Disadvantages of this technique are that it can only be performed on a small section and outside the operation room[38]. Another technique which is currently in development and clinically tested is fluorescent imaging. Fluorescent agents such as folate-FITC, 5-aminolevulinic acid (5-ALA), indocyanine green (ICG), and OTL38 are intravenously injected or orally taken in by the patient. These fluorescent agents accumulate in malignant tumour cell and can be detected by an imaging system intraoperatively. Disadvantages of this technique are that mild adverse effects of OTL38, 5-ALA and folate-FITC such as gastrointestinal disorder, nausea, vomiting, effusion, lose of apatite, diarrhoea and abdominal pain can occur when the agents is taken in [47][25][51][15][41], and the low specificity of ICG [46][39][48].

In other oncological fields, hyperspectral imaging (HSI) is also used as an imaging technique to detect malignant tissue. Hyperspectral imaging captures several reflectance images in contiguous spectral bands of the underlying tissue. The measured reflectance is related to the absorption and scattering properties of the illuminated tissue. This spectral signature of the underlying tissue can be used for the classification of tumour and non-tissue [11][27][20]. Compared to fluorescent imaging, HSI does not need an imaging agent and is therefor label-free, non-invasive, non-contact and non-ionising [13][21]. The first clinical trials suggest that HSI has comparable results as OLT38 and 5-ALA and outperforms ICG. Furthermore, HSI is significantly faster than average intraoperative pathologist consult (5 min vs 45 min respectively)[13] and can scan an entire surface, which can't be done with other pathological margin detection techniques with the same accuracy as HSI such as cryosection (accuracy of 84%–98%). Also, HSI has the potential to be performed in the operating room, which could allow near real-time diagnostic feedback of the resected specimen to the surgeon [26][7][20][21].

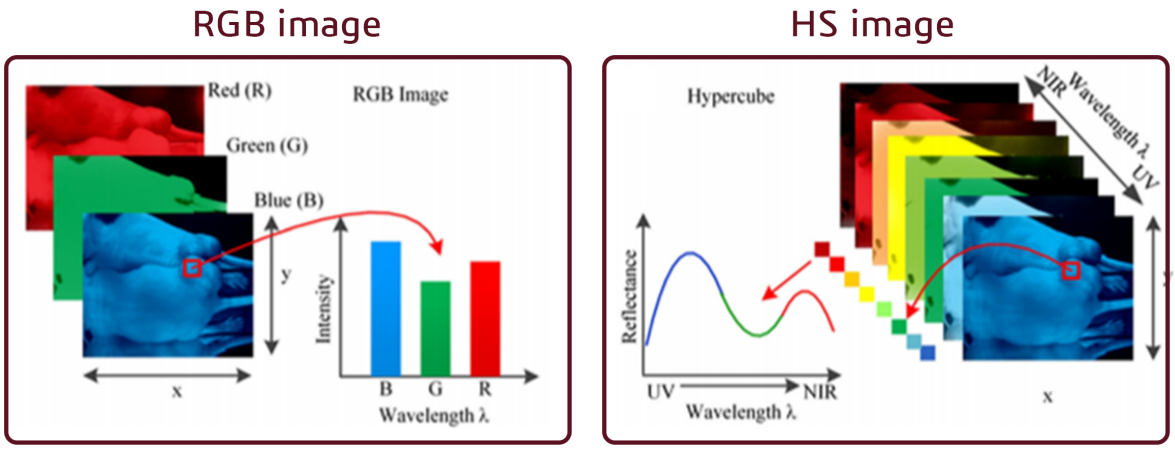

Figure 1.3: Difference between RGB image and HS image: An RGB image consists of 3 wavebands red (564–580 nm), green (534–545 nm) and blue (420–440 nm). An HSI consists of narrow contiguous and adjacent spectral bands(adapted from [30]).

1.4. Study aim

Hyperspectral imaging is a promising technique to detect malignant tissue. Nevertheless, to the best of our knowledge, studies about the feasibility and performance of hyperspectral imaging for the detection of malignant ovarian cancer metastasis are still limited. The aim of this study is to determine the feasibility of malignant ovarian cancer metastases detection using NIR HSI ex vivo.

The research questions are:

- What is the workflow of malignant ovarian cancer metastases detection using HSI?
- What is the performance of malignant ovarian cancer metastases detection using HSI?
- What is the difference in performance of malignant ovarian cancer metastases detection using HI compared to current used or developed techniques?
- What are the knowledge gaps and future direction of malignant ovarian cancer metastases detection using HSI?

The outcome and design of this pilot can be used future use of hyperspectral imaging during cytoreductive surgery to detect malignant ovarian cancer metastases intraoperative and accomplish complete resection of tumour tissue.

2

Method

To evaluate the performance of HSI in ovarian cancer metastases, an ex vivo observational pilot study was done on resected specimen after cytoreductive surgery. The non-WMO research protocol was approved by Erasmus MC, Rotterdam, Netherlands, and can be found in Appendix A. The approach of this study consists out of several steps, including data acquisition, preprocessing, feature extraction, classification with pathological ground truth, training SVM classifier and classification with trained SVM classifier. The steps will be discussed in this chapter.

2.1. Data acquisition

Participants

The recruitment of participants took place at Erasmus MC, Rotterdam, the Netherlands. Patients with the age of 18 years and older with known or high clinical suspicion of primary ovarian cancer planned for either primary cytoreductive surgery (PCS) or interval cytoreductive surgery (ICS), and who were able and willing to comply with the study procedure were enrolled into the study. All participants signed an informed consent before any study-related procedure was performed (see Appendix B for informed consent).

Instrumentation

The hyperspectral (HS) images were acquired with a hyperspectral camera containing a snapshot mosaic 5x5 hyperspectral imaging sensor (IMEC, Leuven, Belgium). This camera can capture an entire scene containing multi-spectral imaging at video rate. The CMOS sensor captures 25 spectral bands with a spectral bandwidth of <15 nm in the NIR range (665-975nm). The spectral bands are arranged in a 5x5 mosaic grid and have a spatial resolution of 409x218 for each band and a total resolution of 2050x1080. The hyperspectral camera is controlled with a desktop PC. The parameters were set at a frame rate of 10 HS cubes per second, an exposure time of 10 milliseconds and a colour gain of 10. The camera and several halogen light sources to illuminate the samples were mounted on a vertical rigid stage. The halogen lights were placed under an angle of 45° to minimise glare pixels. The samples were placed on the black paper underneath the camera. The system is illustrated in Figure 2.1.

Protocol

After cytoreductive surgery, the resected specimen of the ovaries, fallopian tubes, uterus, omentum and/or part of the intestines were brought to the pathology department. From each resected organ, one tissue slice of 20x40x3 mm containing both tumour and non-tumour tissue was taken and placed on black paper. If the tissue contained no tumour tissue, a slice containing only non-tumour tissue was taken and placed on black paper. First, an RGB image was collected with a normal camera, thereafter a light reference image, a dark reference image and HS images of the tissue were collected with the HS camera. After the imaging procedure, the tissue samples were placed on a macro cassette, placed in formaldehyde and processed according to standard protocol.

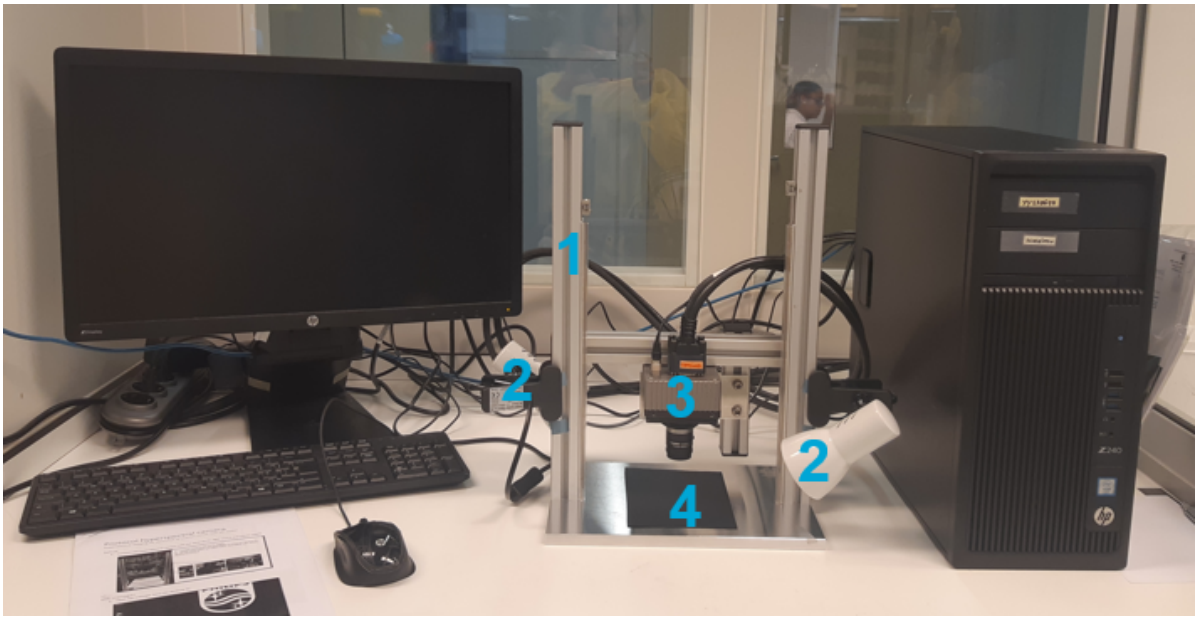

Figure 2.1: Hyperspectral data acquisition system: 1. Vertical rigid stage 2. Halogen light source 3. Hyperspectral camera 4. Plateau with black paper

2.2. Preprocessing of hyperspectral data

All hyperspectral data was preprocessed by image calibration, min-max normalisation and noise filtering. Preprocessing was done with the use of Python and MATLAB (Mathworks Inc.) software. The Python and MATLAB code can be found in Appendix C.

Image calibration

Image calibration calculates the relative reflectance and corrects for the signal variation between images due to the non-uniform illumination system and the focal plane array of the camera (pattern noise). The raw data is calibrated by using a white reference image and a dark reference image. The dark reference image was acquired by the HS system by keeping the shutter of the camera closed and is used to account for the internal noise, caused by the dark current. The white reference image was acquired by taking a picture of a white paper and is used to account for the light distribution. This ensures the consistency and reproducibility of data, independent of the surroundings [9][26][35]. The relative reflectance image is calculated using the following formula:

$$I_{ref}(x,y,\lambda) = \frac{I_{raw}(x,y,\lambda) - I_{dark}(x,y,\lambda)}{I_{white}(x,y,\lambda) - I_{dark}(x,y,\lambda)} \tag{2.1}$$

Where $I_{ref}(x,y,\lambda)$ is the relative reflectance image, $I_{raw}(x,y,\lambda)$ is the raw spectral image, $I_{dark}(x,y,\lambda)$ is the dark reference image, and $I_{white}(x,y,\lambda)$ is the white reference image at the sample pixel location (x,y) and wavelength band λ [26].

Min-max normalisation

Min-max normalisation normalises the range of all features by re-scaling the range of the data to the interval $[min(x_{new}), max(x_{new})]$ and corrects for disproportional feature contributions due to tissue morphology effects. This ensures that the classification algorithm will perform classification based on the shape of the spectral signature and not the amplitude [9]. The normalised image is calculated using the following formula:

$$\hat{x_i} = \frac{x - min(x_i)}{max(x_i) - min(x_i)} * (max(x_{new}) - min(x_{new})) + min(x_{new}) \tag{2.2}$$

Where $\hat{x_i}$ is the normalised image, x the relative reflectance image, $min(x_i)$ the minimum value of x, $max(x_i)$ the maximum value of x, $min(x_{new}$ the new minimum value of x and $max(x_{new}$ the new maximum

value of x [43]. When the image is normalised by re-scaling the range of the data to the interval [0,1], the formula converges to the following formula:

$$\hat{x_i} = \frac{x_i - min(x_i)}{max(x_i) - min(x_i)} \tag{2.3}$$

Noise filtering

Raw HS images can contain pixels that do not contain useful spectral information for tissue classification and reduce the performance of the system, such as background pixels and glare pixels. Several images under different configurations were taken with the hyperspectral camera and images with the least glare were included in the data set. The remaining glare pixels and background pixels were removed from the hypercube by intensity thresholding. Furthermore, the hypercube was divided into a grid of 20x20 pixels. Within each block, the spectra were averaged to increase the robustness to spectral noise and decrease the computational time.

2.3. Patholgical ground truth

The pathological diagnosis was used as the golden standard to label the spectral images. A few days after the operation, the tissue slices were processed in hematoxylin and eosin (H&E) and digitised. The digitised histological images of all specimen were annotated to outline tumour tissue, connective tissue, ovarian stromal tissue, fat tissue, lymphoid tissue, necrotic tissue, epithelial tissue of the intestines and muscle tissue by an experienced pathologist. Areas which were difficult to classify into one group were left out. The annotated images were transformed to the same configuration as the RGB image via a non-rigid registration algorithm in MATLAB (Mathworks Inc.) with approximately 20 control points. This was also done with the HSI. In this way, the HSI and masks have the same configuration. The area of the tumour tissue and the area of non-tumour tissue were selected via HSV colour thresholding to make a tumour tissue and non-tumour tissue mask. These masks served as ground truth for the classification of the HS images. To obtain the labelled tumour and the non-tumour HS images for training the SVM classifier, the HS images were multiplied by the tumour mask and non-tumour mask respectively. Thereafter, the HS images were patched and features were extracted. The workflow can be seen in Figure 2.2.

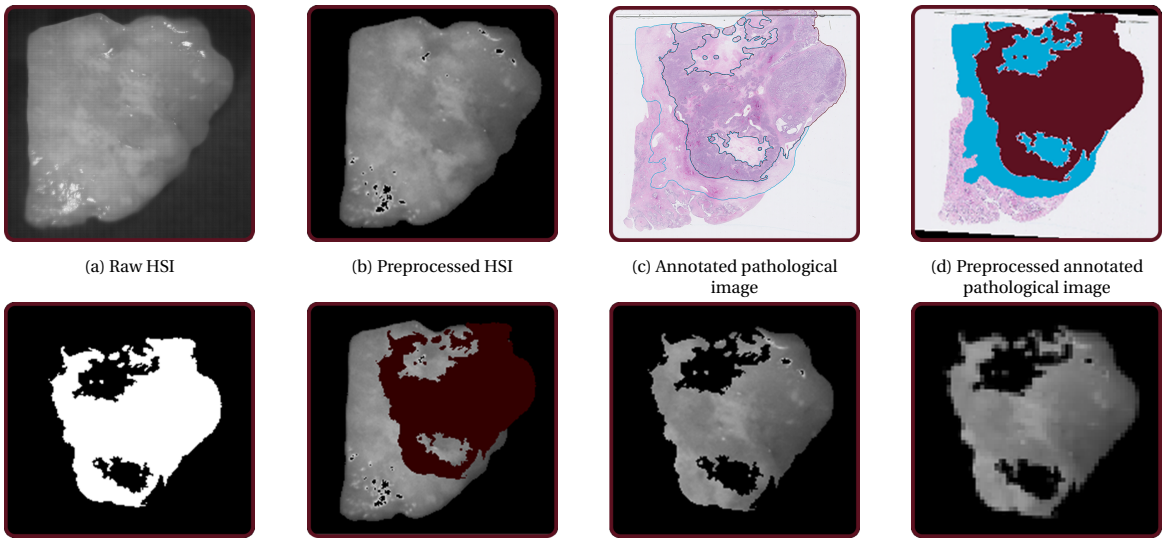

(a) Raw HSI (b) Preprocessed HSI (c) Annotated pathological image (d) Preprocessed annotated pathological image

(e) Tumour mask (f) Tumour mask on HSI (g) Tumour tissue (h) Patched tumour tissue

Figure 2.2: Workflow (a.) The HS images were acquired after cytoreduction. (b.) HS images were preprocessed by calibration, min-max normalisation and noise filtering and transformed (c.) The digitised pathological images were annotated. (d.) The annotated images were transformed. Tumour tissue was filled with the colour bordeaux and the non-tumour tissue was filled with the colour blue. (e.) Tumour tissue and non-tumour tissue were selected via HSV colour thresholding to make masks (f.) Selection of the tumour tissue and non-tumour tissue was made with the mask (g.) The HS images were multiplied by the mask to obtain tumour tissue and non-tumour tissue (h.) The HS images were patched and features were extracted.

2.4. Classification of hyperspectral data

Feature extraction

The HS camera captures 25 reflectance images in adjacent spectral bands of 15 nm. The intensities, derivatives and normalised intensities were extracted and formed the feature set.

Support vector machine classifier

The support vector machine (SVM) classifier with linear kernel function (linear SVM) and Gaussian radial based kernel function (RBF SVM) were used to classify tumour tissue and non-tumour tissue. The SVM classifier finds the best hyperplane that separates the data points of tumour tissue from the non-tumour class with the largest margin between the hyperplane and any data point. For inseparable classes, the objective is the same, but the algorithm imposes a penalty on the length of the margin for every observation that is on the wrong side of its class boundary. The support vectors are the data points that are closest to the separating hyperplane.

The optimal hyperplane for the linear SVM can be determined as the solution of the following dual problem:

$$\begin{cases} \text{Maximise: } \sum_{i=1}^{N} \alpha_i - \frac{1}{2} \sum_{i=1}^{N} \sum_{j=1}^{N} \alpha_i \alpha_j y_i y_j (x_i, x_j) \\ \text{Subjected to: } \sum_{i=1}^{N} \alpha_i y_i = 0 \text{ and } 0 \leq \alpha_i \leq C, i = 1, 2, ..., N. \end{cases} \tag{2.4}$$

The discriminant function associated with the hyperplane is defined as:

$$f(x) = \sum_{i \in S} \alpha_i y_i (x_i, x) + b \tag{2.5}$$

Where α_i are the Lagrange multipliers, x_i is set of data points with their labels y_i, C is a constant representing the regularisation parameter to control the penalty assigned to errors and S is the subset of training sample corresponding to nonzero Lagrange multipliers α_i [32].

The optimal hyperplane for the non-linear SVM can be determined as the solution of the following dual problem:

$$\begin{cases} \text{Maximise: } \sum_{i=1}^{N} \alpha_i - \frac{1}{2} \sum_{i=1}^{N} \sum_{j=1}^{N} \alpha_i \alpha_j y_i y_j K(x_i, x_j) \\ \text{Subjected to: } \sum_{i=1}^{N} \alpha_i y_i = 0 \text{ and } 0 \leq \alpha_i \leq C, i = 1, 2, ..., N. \end{cases} \tag{2.6}$$

The discriminant function associated with the hyperplane is defined as:

$$f(x) = \sum_{i \in S} \alpha_i y_i K(x_i, x) + b \tag{2.7}$$

Where K is the kernel function. The kernel for the Gaussian radial based function is defined as $K(x_i, x) = exp(-\gamma ||x_i - x||^2)$ [32].

K-nearest neighbour classifier

The k-nearest neighbour (k-NN) classifier finds the nearest k data points x_i to the test sample y according to a given distance measure, such as the Euclidean distance. Majority voting is employed to assigns the class label to the test sample [23]. The Euclidean distance can be calculated by:

$$d(x_i, y) = ||x_i - y||_2^2 \tag{2.8}$$

To compensate for the unbalanced data-set, weighting factors have been assigned to the tissue classes in all classifiers.

2.5. Performance of classifiers

Training and validation of the classifiers

The SVM classifiers were validated using leave-one-out cross-validation. The classification algorithm was trained on a training set of all spectral images from 9 of the 10 patients with the known class label, based on the pathological ground truth. The patient who was left out was used in the validation data set. The binary classified images from the test set were compared with the pathological ground truth to determine the performance of the classifier.

Performance metric

The performance of the classifiers was evaluated with sensitivity, specificity, positive predictive value (PPV) and negative predicted value (NPV) based on the confusion matrix of the optimal threshold point of the receiver operating characteristic (ROC) curve. The optimal threshold point of the ROC curve was calculated by using the maximal Youden index. The sensitivity defines how many correct tumour pixels are classified along all classified tumour pixels. The specificity defines how many correct non-tumour pixels are classified along all classified non-tumour pixels. The PPV defines how many correct tumour pixels are classified along all predicted tumour pixels. And the NPV defines how many correct non-tumour pixels are classified along all predicted non-tumour pixels. The sensitivity, specificity, PPV and NPV and can be determined using the following equations:

$$Sensitivity = \frac{TP}{TP+FN} \tag{2.9}$$

$$Specificity = \frac{TN}{TN+FP} \tag{2.10}$$

$$PPV = \frac{TP}{TP+FP} \tag{2.11}$$

$$NPV = \frac{TN}{TN+FN} \tag{2.12}$$

Because the sensitivity, specificity, PPV and NPV are dependent on the threshold value of the ROC curve, the area under the ROC curve (AUC) and the Matthews correlation coefficient (MMC) have been calculated to represent the scalar measurement for the quality of the classification. The AUC represents how good the model is in distinguishing between two classes, in this case, tumour tissue and healthy tissue. A perfect classifier has an AUC of 1, a classifier that randomly assigns observations to a class has an AUC of 0.5. The MCC returns a value from 1 to 1, where 1 indicates a perfect prediction, 0 means no better than randomly prediction and 1 indicates a total disagreement between prediction and ground truth. The MMC is determined using the following equation:

$$MCC = \frac{TPxTN - FPxFN}{\sqrt{(TP+FN)(TP+FN)(TN+FP)(TN+FN)}} \tag{2.13}$$

Where $TN(T)$ is true negative, $TP(T)$ is true positive, $FP(T)$ is false positive, and $FN(T)$ is false negative dependent of the threshold value T [26].

3

Results

3.1. Participants and pathology

In total 11 patients were enrolled in the study. The mean age was 58 years (median:58, range 30-78). Eight patient underwent interval debulking operation and three patients primary debulking operation. Eight patients presented high-grade serous adenocarcinoma, one patient low-grade serous adenocarcinoma, one patient serous carcinoma and one patient high and low-grade mucinous adenocarcinoma. Eight patients had a FIGO stage IV ovarian cancer, three patients had FIGO stage IIIC ovarian cancer. In total ten patients were included in the study. Patient 5 was left out because the primary location of the tumour was uncertain. The patient characteristics can be seen in Tabel 3.1.

Table 3.1: Patient characteristics

Patient number	**Age**	**Primary location**	**Histology**	**Grade**	**FIGO Stage**	**Procedure**	**Tissue type**
1	72	Ovarian	Serous adenocarcinoma	3	IIIC	PDS	A: Ovarian, B: Ovarian C: Ovarian, D: Omentum
2	78	Ovarian	Serous carcinoma		IV	IDS	A: Mesenterium
3	64	Ovarian	Serous adenocarcinoma	3	IV	IDS	A: Omentum, B: Ovarian
4	56	Ovarian	Serous adenocarcinoma	3	IV	IDS	A: Omentum, B: Omentum C: Intestines
5	56		Mucinous adenocarcinoma	1 / 3	IV	PDS	A: Omentum
6	67	Ovarian	Serous adenocarcinoma	3	IIIC	IDS	A: Ovarian, B: Ovarian C: Intestines, D: Omentum E: Omentum
7	58	Ovarian	Serous adenocarcinoma	3	IV	IDS	A: Omentum, B: Ovarian C: Ovarian
8	65	Ovarian	Serous adenocarcinoma	3	IIIC	IDS	A: Omentum, B: Ovarian
9	46	Ovarian	Serous adenocarcinoma	3	IV	IDS	A: Ovarian B: Ovarian
10	50	Ovarian	Serous adenocarcinoma	3	IV	IDS	A: Ovarian, B: Omentum C: Ovarian
11	30	Ovarian	Serous adenocarcinoma	1	IV	PDS	A: Omentum

PSD:Primary debulking surgery, IDS: interval debulking surgery

3.2. Spectral signature

In this study, 27 tissues samples were imaged, including tissue from the ovarian (13 samples), omentum (11 samples), mesenterium (1 sample) and intestines (2 samples). All the processed tissue samples can be seen in Appendix D. The samples contained different tissue types such as connective tissue, necrotic tissue, ovarian stromal tissue, adipose tissue, lymphoid tissue, muscle tissue, epithelial tissue of the intestines and tumour tissue. In Figure 3.1a spectral signature of the different tissue types can be seen. For the classification of tissue, the tissue types connective tissue, necrotic tissue, ovarian stromal tissue, adipose tissue, lymphoid tissue, muscle tissue and epithelial tissue of the intestines were grouped in the non-tumour tissue class. In Figure 3.1b, the average spectra of these tissue types combined are shown.

The measured spectra for all tumour tissue differed significantly (P<0.005) from that of non-tumour tissue except the spectra with the wavelength of 786 nm, 930 nm and 943 nm. The spectra showed large within-class variations which may primarily be attributed to the heterogeneity. The measured reflectance is related to the absorption and scattering properties of the illuminated tissue e.g. cellular crowding, amount of blood flow and metabolic activity, substrates and type of tissue [4]. This can be seen as intensity dips in the spectral signature [11][27]. The NIR region has several scattering dominant region for biological tissues such as fat lipids, collagen, and water. When we look at Figure 3.1 we see a relatively low-intensity value after 923 nm for non-tumour and tumour tissue. An explanation can be due to the lipid absorption peak around 930 nm. We also see a small intensity dip at 760 nm in non-tumour tissue. This can be due to the presence of deoxygenated blood [17][42].

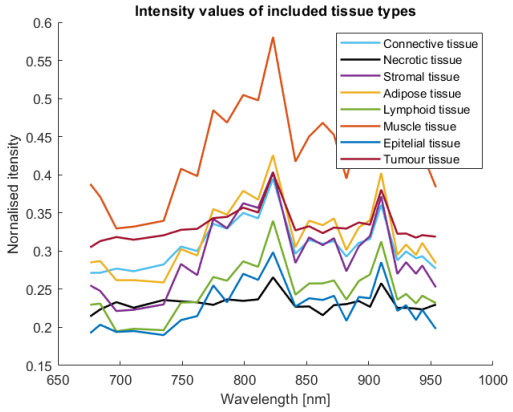

(a) Intensity value of included tissue types types

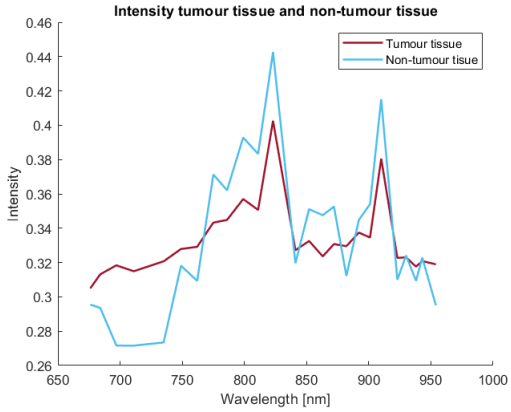

(b) Intensity value of tumour tissue and non-tumour tissue

Figure 3.1: Intensity value of included tissue types

3.3. Tissue classification

Feature selection

The feature set consisted out of 674 features. The p-score of these features can be seen in Appendix E. The features with a p-score >0.05 were removed from the data set. The most influencing features have been chosen for the classification of tumour tissue and non-tumour tissue. In total 19 of the 674 features were selected for the classification of tumour tissue and non-tumour tissue. Box-plots of the most relevant features can be seen in Figure 3.2. The features included were the intensities 697 nm, 775 nm, 799 nm, 823 nm, 863 nm, 872 nm, 901 nm, 910 nm, 923 nm, the derivatives between 684-697 nm, 882-892 nm, 923-930 nm, 943-954 nm and the normalised intensity of 676/910 nm, 697/910 nm, 762/910 nm, 872/910 nm, 923/910 nm, and 930/910 nm.

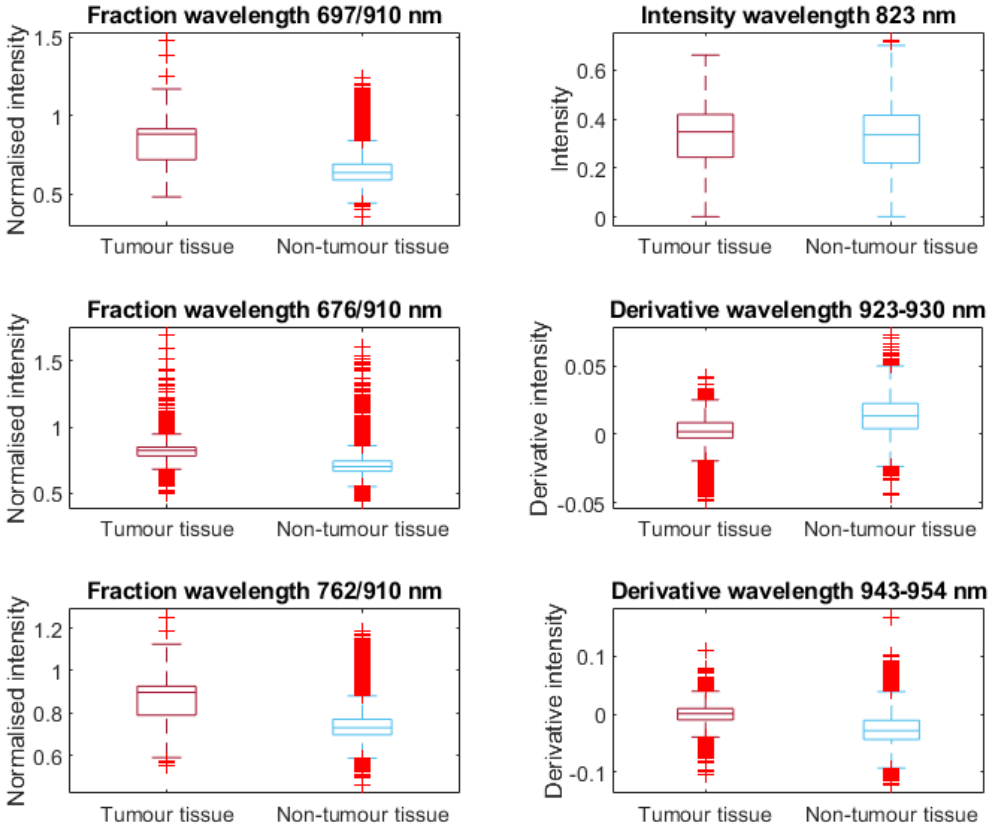

Figure 3.2: Boxplots of the most relevant features

Performance of the classifiers

In Table 3.2, classification results of tumour tissue and non-tumour tissue with the use of the linear SVM, RBF SVM, and k-NN classifiers can be seen. The linear SVM had the best results with a sensitivity of 0.806, specificity of 0.747, PPV of 0.530, NPV of 0.816, AUC of 0.827 and MCC of 0.412. The second was the RBF SVM classifier with a sensitivity of 0.836, a specificity of 0.725, PPV of 0.502, NPV of 0.799, AUC of 0.836 and MCC of 0.386. The classification result of the k-NN classifier was slightly lower compared to the SVM classifiers and had a sensitivity, specificity, PPV, NPV, AUC and MCC of 0.675, 0.722, 0.474, 0.735, 0.722, and 0.268. The full results can be seen in Appendix F. The data set of patient 2,3 4, and 8 only consisted out of non-tumour tissue, therefore it was only included in the training set.

Table 3.2: Performance of the classifiers

Classification method	Sensitivity	Specificity	PPV	NPV	AUC	MCC
Linear SVM	0.806	0.747	0.530	0.816	0.827	0.412
RBF SVM	0.836	0.725	0.502	0.799	0.836	0.386
k-NN	0.675	0.722	0.474	0.735	0.722	0.268

4

Discussion

The most important prognostic factor for the survival of advanced-stage ovarian cancer is the complete resection of all microscopic tumour tissue during cytoreductive surgery[24]. Still, even after complete CRS and removal of all visible and palpable tumours, more than two-thirds of women with advanced-stage ovarian cancer experience recurrence due to microscopic residual tumour. Therefore, an intraoperative visualisation technique is of great importance to detect these microscopic tumours. In this pilot study, the feasibility of NIR hyperspectral imaging for the detection of malignant ovarian cancer metastases was tested ex vivo. The linear SVM classifier had the highest performance with a sensitivity of 0.81, a specificity of 0.75, AUC of 0.83 and MCC of 0.41 for the detection of tumour tissue. The second best was the RBF SVM classifier which had a sensitivity of 0.84, a specificity of 0.72, AUC of 0.84 and MCC of 0.39. And last was the k-NN classifier with a sensitivity of 0.68, a specificity of 0.72, AUC of 0.72 and MCC of 0.27.

4.1. Comparison to current used or developed techniques

When we compare the results of HSI with the commonly used intraoperative cryosection diagnosis, discussed in the study of Palakklan et al. [38], we see that hyperspectral imaging still performs less accurate than cryosection. During cryosection a small piece of the suspicious tissue is sent to the pathology lab where it is frozen, sliced in sections and microscopically examined by the pathologist. The study of Palakklan et al. [38] found a sensitivity of 0.90, a specificity of 0.97, PPV of 0.90 and NPV of 0.97 for malignant ovarian tumours, which is significantly higher than the results found in this study. Nevertheless, HSI has a faster imaging time. Classification only took several seconds in our study, where cryosection takes approximately 20 minutes. Also, HSI can scan a whole area, where cryosection can only be applied on a small resected area outside of the operation room [13][21][7]. In the study of Hoogstins et al.[15] and Randall et al.[41], intraoperative fluorescent imaging with the use of the fluorophore OTL38 was evaluated. OTL38 is active fluorescent agents which target folate receptors. The study of Randall et al. [41] found a sensitivity of 0.84, a specificity of 0.12, PPV of 0.85 and NPV of 0.10 in patients with ovarian cancer when no correlation between lesions within patients was assumed. The sensitivity is slightly better in comparison with the current study, but the specificity was lower. This was especially in lymph nodes (52%), likely due to active macrophages with FR-β receptors which are also a binding receptor of OTL38. Other locations of false positives were to FR-α on the apical membrane of noncancerous epithelial cells in the uterus and fallopian tubes [15]. OTL38 also gave several mild adverse events such as gastrointestinal disorder, nausea, vomiting and abdominal pain (18.2%) [15][41], infusion-related reactions (11.4%) sneezing and increase lacrimation (2.3%) [41], which is not the case for HSI. In the studies of Liu et al.[25] and Yonemura et al.[51], intraoperative fluorescent imaging with the use of the fluorophore 5-ALA was evaluated. 5-ALA is a pro-drug, precursor of protoporphyrin IX and is enzyme-activated/micro-environment activated agent. Also here a higher performance compared to the current study was found. In the study of Liu et al.[25], a sensitivity of 0.93, a specificity of 1.00, PPV of 1.00 and NPV of 92.5 for the detection of peritoneal metastases from ovarian cancer and primary peritoneal cancer was found. In the study of Yonemura et al.[51] a sensitivity of 0.89, a specificity of 1.00, PPV of 1.00 and NPV of 0.90 for the detection of peritoneal metastases from epitelial ovarian cancer was found. Nevertheless, some small adverse effects occurred during the intake of 5-ALA such as pleural effusion (n=2), loss of

appetite (n=1), diarrhoea (n=1), abnormal lab results [25], nausea (n=1) and vomiting (n=1) [25][51] In the studies Tummers et al.[46], Pop et al.[39], and Veys et al.[48], the intraoperative fluorescent imaging with the use of the fluorophore ICG was evaluated. ICG binds to serum proteins and passively accumulates in tumour tissue due to the enhanced vascular permeability and retention (EPR) effect. HSI had a better performance than fluorescent ICG due to the low sensitivity of the EPR effect. In the study of Tummers et al.[46] a sensitivity of 1.00 and a specificity of 0.38 was found for patients with ovarian cancer. The study of Pop et al.[39] found a sensitivity of 0.80, a specificity of 0.41, PPV of 0.03 and NPV of 0.99 for retroperitoneal lymph nodes. The study of Veys et al.[48] found a sensitivity between 0.50-0.73, specificity between 0.50-0.57, and PPV of 0.57-0.77 for peritoneal residual scar tissue or malignant ovarian tumour tissue.

In most of the mentioned studies, there are differences in tumour types, FIGO stages and study designs included in the data set in comparison with the current study. This could alter the performance and does not represent a perfect comparison between the current study and other studies in the field of intraoperative detection of malignant ovarian cancer metastases. Nevertheless, it gives a good comparison of what is already done in the field and what the target performance needs to be. For now, 5-ALA is the biggest competitor for intraoperative visualisation. Cryosection has a very good performance but is not suitable for real-time intraoperative visualisation of a whole are. There are also other intraoperative detection techniques for the detection of malignant ovarian cancer metastasis such as Raman imaging (SERS or SERRS) [18][37], autofluorescent imaging and reflectance spectroscopy [29][45], gamma probes [6][49], intraoperative MRI [22], intraoperative ultrasound [33], touch impression cytology [19], other fluorescent agents (single-walled carbon nanotubes, quantum dots and lanthanide-based nanoparticles) [49][28], and more [44]. These are not clinically tested yet.

4.2. Limitations and recommendations

This pilot study had several limitations which are listed in the following.

Data set

This study contained a limited data set for training of the classifier. It is not yet known if there is any difference in performance for other histological types, tissue types, procedures or premenopausal/postmenopausal patients[34]. The influence of these characteristics on the performance still needs to be investigated.

Hyperspectral camera

The HS camera contains a snapshot mosaic 5x5 hyperspectral imaging sensor (IMEC, Leuven Belgium) which can capture an entire scene in a few seconds without spatial and spectral aliasing artefacts. It is therefore capable of imaging moving object, which is useful for future in vivo use [11]. The drawbacks of this camera are that it has a lower spatial and spectral resolution compared to whisk-broom (point-scanning) cameras, push-broom (line-scanning) cameras, spectral scanning (area-scanning or plane-scanning) cameras, and only has 25 spectral bandwidths of <15 nm. This makes in detail research of optical tissue properties more difficult, due to less feature extraction [11].

The camera captures images in the NIR range from 665 nm till 975 nm. In this region, several chromophores such as blood, water, melanin, fat, bilirubin, and beta-carotene contribute to the absorption of light and therefore the spectral signature of diverse tissues [17]. In this study, an intensity dip in the spectrum of non-tumour tissue can be seen at 760 nm (see Figure 3.1). This can be due to the presence of deoxygenated haemoglobin, which has an absorption peak at 760 nm. What stands out is that the spectral signature of tumour tissue does not have this dip, which was not expected due to angiogenesis in tumour tissue. Also around 930 nm, an intensity dip in non-tumour tissue can be seen. This can be due to the presence of adipose tissue such as tissue from the omentum. When we compare the spectral signature of this study to other studies[2][3][14], we see a dip between 850 nm and 900 nm in the spectrum of this study which is not present in the other studies. The dip is present in all tissue types and can be due to noise in the system. Because all the tissue types are subjected to the noise, it does not affect the outcome within this data set, only when compared to outcomes with the use of other systems.

An advantage of the NIR wavelength range of the camera is that it can measure up several millimetres and is scattering dominant for biological tissue, which leads to more detectable differences between tissue

types [11][7][10][21]. The visual (VIS) wavelength range for the detection of tumour tissue is also evaluated in the study of Baltussen et al.[2] and Kho et al. [20]. Both studies found that the combination of VIS and NIR wavelength range had the best result, because of the combined features that can be made. However, in in vivo studies, the visual wavelength range (400-700 nm) which is scattering dominant for haemoglobin, is not preferred due to the presence of blood [17][2]. The study of Beaulieu et al. [4] also looked into the use of the SWIR wavelength range (900-2500 nm) and found that the performance was significantly better in comparison to the combined visual and NIR wavelength range and suggest that there may be tumour specific signals in the SWIR wavelength range. According to [17], the SWIR wavelength has scattering dominants for water and adipose tissue. This can be of added value for the detection of tumour tissue in adipose regions such as the omentum.

Histological discrepancies

The annotated tumour tissue contained largely tumour but also included small amounts of connective tissue, calcification and other types of non-tumour tissue. This influences the performance of the classifier negatively. Furthermore, there was a discrepancy between the measured volume of the HS camera and the pathological ground truth. The HS camera can image a volume of a few millimetres, but the H&E section only provides information about the superficial cell layers [10][20][21]. In addition, for the first 4 patients, the bottom of the tissue slide instead of the top of the tissue slide was inspected due to the wrong configuration of the tissue in the pathological tray.

Preprocessing errors

During noise reduction, most of the background pixels and glare pixels were removed. Nevertheless, not all the pixels were removed due to the differences in HSV value of the background. In some cases, also some parts of the tissue were removed. Furthermore, normalisation was done before noise filtering. To enhance the influence of normalisation, normalisation as last step can be tried.

Registration errors

Registration errors occurred when the pathological ground truth was registered on the HS image, due to tissue-deformation during the tissue processing. During this study, non-rigid registration algorithm was used with approximately 20 control points. In this method, elastic deformation within the tissue is not accounted for. This can be included in future studies. The study of Kho et al.[20] tried to lower the discrepancies between the histological ground truth and HSI by adding a group where all the tissue edges were removed up to 1 mm from the edge. Edges are more likely to contain mixed spectra due to errors in histological annotation because of the small pixel size, registration errors, discrepancies between the measured volume of HSI and H&E and influence of the surrounding reflectance spectra on the pixel. In general, the classification performance of the data set where the edges were removed was higher than in the data set where the edges were not removed.

Feature extraction

For the feature extraction, only the intensity, derivative and the normalisation were used. Furthermore, not all possible combinations between the features were made. First, the best derivatives were selected, thereafter the best intensities, then the best norm was selected and the best wavelengths of this norm were added. In the future, a principle component analysis (PCA) or other feature selection procedures can be used to optimise this procedure and find new features.

Classifier

In this study, the linear SVM, RBF SVM, and k-NN classifiers have been evaluated. The linear SVM classifier had the best results, closely followed by the RBF SVM classifier, and last was the k-NN classifier. Based on these results, the linear SVM classifier would be good for future research. Nevertheless, the data was limited and more research needs to confirm these results. In the future, other classification methods can be investigated for the classification of ovarian cancer. In literature, several other classifiers have been used to classify tumour tissue. In the study of Lu et al.[26], QDA, linear discriminant analysis (LDA), ensemble LDA, RBF SVM, and random forest (RF) were evaluated for the detection of head and neck squamous cell carcinoma. Ensemble LDA had the overall best performance followed by LDA, linear SVM, RF, RBF SVM and last quadratic discriminant analyse (QDA). The study of Maktabi et al.[27] compared the RF, SVM, multilayer per-

ceptron (MLP) and k-NN classifiers. They found that the SVM classifier with oversampling performed best in two tissue classification of oesophageal carcinoma. In the study of Halicek et al.[12] convolutional neural network (CNN) based classifiers were compared with the SVM based classifiers. CNN based classifiers outperformed SVM based classifiers in the classification of neck squamous cell carcinoma. Fabelo et al.[9] compared CNN, deep neural network (DNN) and SVM based classification algorithm with each other. The DNN algorithm achieved the best results in the binary classification of glioblastoma. However, deep learning can be prone to over-fitting if there is insufficient data, and the results can be more difficult to interpret [11].

To compensate for the unbalanced data-set, weighting factors were implemented during classification which assigns different weights to tissue classes[21]. Other methods that can be used are oversampling, which generate synthetic samples based on the k-nearest neighbour [27] and under-sampling which randomly select as many spectra as the smallest class [4]. The use of weighting factors has been chosen over under-sampling due to the limited data set.

4.3. Future direction

This pilot study is done as a first step towards hyperspectral imaging for the detection of ovarian cancer metastasis. The ultimate goal is to use hyperspectral imaging during cytoreductive surgery to detect malignant ovarian cancer metastases intraoperatively and accomplish complete resection of tumour tissue in a short time. However, before HSI can be implemented in real practice, further validation in vivo is required. The environmental factors change during in vivo evaluation which change the spectral signature of the tissue and can influence the performance. Also, the workflow will change during cytoreductive surgery when hyperspectral imaging is implemented. Questions about the ease of use, time of use, the learning curve of the new device, and the cut off value for the procedure may rise. Furthermore, the intraoperative device still needs to be developed. Trade-offs between the precision of the system versus the cost of the system need to be made.

5

Conclusion

All in all, this pilot study shows that HSI is a promising technique that can improve the detection of malignant ovarian metastasis and increase the progression-free survival of patients with ovarian cancer. The linear SVM classifier had the highest performance with a sensitivity of 0.81, a specificity of 0.75, AUC of 0.83 and MCC of 0.41 for the detection of tumour tissue. When we compare the results of HSI with the commonly used intra-operative cryosection diagnosis, we see that cryosection still performs more accurate than HSI. Nevertheless, HSI can scan a whole area, is faster, non-contact and non-invasive and can be used inside the operation room. When we compare HSI to fluorescent imaging we see that HSI has better accuracy than OTL38 and ICG, but worse than 5-ALA. Nevertheless, some small adverse effects occurred during the intake of 5-ALA.

However, before HSI can be implemented in practice, further validation is required in vivo and technical enhancements need to be made. Future research can focus on enlarging the training data set to enhance the performance of the classifier. The wavelength range of the hyperspectral camera can be enhanced by including the SWIR wavelength range. The SWIR wavelength range might include additional features which can be combined with the relevant features in the NIR wavelength range for better performance. Furthermore, the registration of the pathological ground truth can be enhanced by including a registration algorithm which accounts for elastic deformation. In addition, several feature selection methods can be evaluated to find the optimal features and other classifiers can be evaluated for the detection.

A

Appendix: Research protocol for application non-WMO statement

General data

Title
Hyperspectral imaging for detection of ovarian cancer (HSI-OC study)

Data
27 February 2020

Version
1.0

Author
S.M. Perez
Delft University of technology
Faculty of Mechanical engineering
Biomedical Engineering
Mekelweg 2
2628CD Delft
Tel. +31 0646993742

Coordinating researcher
Dr. H.J. van Beekhuizen, oncologic gynaecologist
Erasmus MC
Na- 1511
Dr. Molewaterplein 40
3015 GD Rotterdam
Tel. 010 703 33 81

Principal investigator
Drs. G.M. Nieuwenhuyzen, oncologic gynaecologist
Erasmus MC
Na-1511
Dr. Molewaterplein 40
3015 GD Rotterdam
Tel. 010 703 33 81

Researchers
Dr. M. Jozwiak, gynaecologist

Erasmus MC
Na- 1511
Dr. Molewaterplein 40
3015 GD Rotterdam
Tel. 010 703 33 81

Prof. Dr. J. Dankelman
Delft University of technology
Faculty of Mechanical engineering
Biomechanical engineering
Room: 34.E-1-330
Mekelweg 2
2628CD Delft
Tel. +31 15 27 85565

S.M. Perez
Delft University of technology
Faculty of Mechanical engineering
Biomedical Engineering
Mekelweg 2
2628CD Delft
Tel. +31 0646993742

Client (provider)
Dept. Gynaecological Oncology Erasmus MC Dept. Biomedical Engineering Delft University of Technology

Research data

Rational
Ovarian cancer is the second most common gynaecologic malignancy, with the highest mortality of gynaecologic cancers. Most women diagnosed with ovarian cancer are diagnosed at an advanced stage (FIGO stage III or IV), where the disease has spread throughout the peritoneal cavity. These women have a 5-year survival of 5-30%. The cornerstone of treatment of ovarian cancer is cytoreductive surgery, combined with systemic chemotherapy to treat microscopic disease. The completeness of cytoreductive surgery is the most important factor for treatment success. Currently the success of surgery is defined by visual inspection by the surgeon. Cytoreduction is considered complete when there is no visible residual tumour left. It is questionable whether this is an objective and optimal measure. As completeness of cytoreductive surgery is the most important predicting factor for treatment success, a better method of visualisation of malignant tissue intraoperatively is needed to optimise the chance for objectively complete cytoreduction in women with ovarian cancer.

Hyper spectral imaging (HSI) has demonstrated potential to become a powerful tool to study and identify several diseases in the medical field, being a non-contact, non-ionizing, and a label-free imaging modality.

Goals
The aim of this pilot study is to determine whether hyperspectral imaging can be used as an imaging tool for the detection of ovarian cancer ex vivo. The outcome and design of this pilot can be used for a follow-up study to determine whether hyperspectral imaging can be used as an imaging tool for the detection of ovarian cancer in vivo.

Study design
Observational study

Study population
Patients with stage III and IV ovarian cancer eligible for cytoreductive surgery.

Inclusion criteria

- Known or high clinical suspicion of primary ovarian cancer planned for either primary cytoreductive surgery or interval cytoreductive surgery by laparotomy
- The subject is able and willing to comply with study procedures. A signed and dated informed consent is obtained before any study-related procedure is performed.
- Age of 18 years and older

Exclusion criteria

- Patients from whom the ovaries, fallopian tubes, uterus, omentum and part of the intestines were removed.

Number of subjects / sample size
10 female participants

Each month, about 3-4 patients with stage III or IV ovarian cancer undergo cytoreduction at Erasmus MC. When we take into account that 75% of the available patients will or can participate, inclusion of 10 patients will most probably take around 3 months.

Recruitment subjects
The recruitment takes place at Erasmus MC. Upon planning of cytoreductive surgery, the patient will be informed about the study. After informed consent is given, the patient will be enrolled.

Intervention

- The selected patient undergoes cytoreductive surgery as planned.
- Immediately after cytoreduction, the ovaries, fallopian tubes, uterus, omentum and/or part of the intestines (if applicable) are prepared for hyperspectral imaging.
- The hyperspectral images of the ovaries, fallopian tubes, uterus, omentum and/or part of the intestines are collected. These resected ovaries, fallopian tubes, uterus, omentum and/or part of the intestines consist of normal tissue and the tumor.
- Also visual images of the ovaries, fallopian tubes, uterus, omentum and/or part of the intestines are collected.
- After imaging, the ovaries, fallopian tubes, uterus, omentum and/or part of the intestines are, according to normal protocol, sent to the pathological laboratory for examination. Pathologic diagnosis and coloring is carried out by a professional pathologist and the results are compared with the hyperspectral images and visual images.

Standard care / standard treatment
This procedure is not yet offered as standard care. In the future, this procedure could potentially be used for visualisation of malignant tissue intraoperatively.

Study parameters

- Comparison of image characteristics from visual images of tumor tissue and healthy tissue
- Comparison of image characteristics from hyperspectral imaging of tumor tissue and healthy tissue
- Comparison of image characteristics from histopathological examination of tumour tissue and healthy tissue
- Concordance of image characteristics of tumour tissue and healthy tissue from hyperspectral images and histopathological examination
- Concordance of image characteristics of tumor tissue and healthy tissue from visual images and histopathological examination

Study endpoints

- Determine the true positive, true negative, false positive and false negative of hyperspectral images compared with histopathological examination
- Determine the accuracy, sensitivity and specificity of the detection of tumour tissue with hyperspectral imaging compared to histopathological examination

Statistical analyses
Accuracy, sensitivity and specificity of the detection of tumour tissue with hyperspectral imaging compared to histopathological examination.

Load for subject
There is no anticipated additional load for the participants since hyperspectral imaging is a non-invasive imaging methods based on the interaction of tissue and light, which is done ex-vivo after the operation and is harmless to the patient.

Risk to the subject
There is no anticipated additional risk for the participants since hyperspectral imaging is a non-invasive imaging methods based on the interaction of tissue and light.

Benefit participation in the research
This study can be used for further development of a visualisation technique of malignant tissue intraoperatively to optimise the chance for objectively complete cytoreduction in women with ovarian cancer. No beneficial effect is expected for the patients participating in this study.

Disadvantages participation in the research
None

Compensation for the subjects
None

Administrative aspects
Data, documents and body materials will be handled according to GCP principles. Data of the participants will be coded and stored in the Erasmus MC and saved for 15 years. Body materials will be saved as usual in the pathology archive.

Publication policy and amendments
The guidelines for publishing and authorship of Erasmus MC will be followed.

Other points of interest for the METc
None

B

Appendix: Informed consent

Gebruik van weefsel van patiënten ten behoeven van het ontwikkelen van een manier voor het beter afbeelden van eierstokkanker bij operaties

Officiële titel: Hyperspectral imaging for detection of ovarian cancer (HSI-OC study)

Inleiding

Geachte mevrouw,

Er is bij u eierstokkanker ontdekt en er is een operatie gepland om de tumor te verwijderen. Wij vragen u hierbij of er een extra test op het verwijderde weefsel gedaan mag worden en of wij de gegevens van uw behandeling mogen gebruiken voor medisch wetenschappelijk onderzoek. U doet dan officieel mee aan het onderzoek. Heeft u na het lezen van de informatie nog vragen? Dan kunt u terecht bij uw behandelend arts of de hoofdonderzoeker die onderaan deze brief vermeld is.

1. Wat is het doel van het onderzoek?

Met dit onderzoek hopen wij een nauwkeurige manier te ontwikkelen om eierstokkanker beter te kunnen zien tijdens een operatie. Deze test wordt gedaan op het weefsel dat bij de operatie wordt verwijderd.

2. Hoe wordt het onderzoek uitgevoerd?

Na de operatie zal het verwijderde weefsel onder een speciale camera worden gelegd. Deze camera maakt foto's van het weefsel. Vervolgens wordt het weefsel op de gebruikelijke manier verzonden en onderzocht door de patholoog. De gegevens van uw behandeling en de uitslag van de patholoog worden gebruikt voor het onderzoek.

3. Wat is meer of anders dan de reguliere behandeling(en) die u krijgt?

De behandeling is voor u hetzelfde als de standaard behandeling. De extra foto's zijn het enige verschil. Verder worden de gegevens van uw ingreep en de uitslag van het onderzoek door de patholoog (gecodeerd) gebruikt voor het onderzoek.

4. Wat zijn mogelijke voor- en nadelen van deelname aan dit onderzoek?

Deelname aan dit onderzoek heeft geen nadelen. Voor de toekomst kan het onderzoek wel helpen de behandeling van vrouwen met eierstokkanker te verbeteren.

5. Wat wordt er van u verwacht?

Van u wordt niks verwacht. Alleen als u toestemming geeft worden uw weefsel en gegevens over uw ziekte bewaard en gebruikt voor dit wetenschappelijk onderzoek.

6. Wat gebeurt er als u niet wenst deel te nemen aan dit onderzoek?

U beslist zelf of u meedoet aan het onderzoek. Deelname is vrijwillig. Als u besluit niet mee te doen, dan tekent u het formulier niet, uw gegevens worden dan niet in het onderzoek opgenomen. U hoeft niet te zeggen waarom u niet wilt meedoen. U kunt uw toestemming ook later nog intrekken.

7. Gebruik en bewaren van uw gegevens en lichaamsmateriaal

Voor dit onderzoek worden uw persoonsgegevens en lichaamsmateriaal verzameld, gebruikt en bewaard. Het gaat om gegevens zoals uw naam, adres, geboortedatum en om gegevens over uw gezondheid. Voor dit onderzoek is gezond en tumorweefsel uit de eierstok nodig. Het verzamelen, gebruiken en bewaren van uw gegevens en uw lichaamsmateriaal is nodig om de vragen die in dit onderzoek worden gesteld te kunnen beantwoorden en de resultaten te kunnen publiceren. Wij vragen voor het gebruik van uw gegevens en lichaamsmateriaal uw toestemming.

Vertrouwelijkheid van uw gegevens en lichaamsmateriaal

Om uw privacy te beschermen krijgen uw gegevens en uw lichaamsmateriaal een code. Uw naam en andere gegevens die u direct kunnen identificeren worden daarbij weggelaten. Alleen met de sleutel van de code zijn gegevens tot u te herleiden. De sleutel van de code blijft veilig opgeborgen in de lokale onderzoeksinstelling. De gegevens en lichaamsmateriaal die naar eventuele andere betrokken partijen worden gestuurd, bevatten alleen de code, maar niet uw naam of andere gegevens waarmee u kunt worden geïdentificeerd. Ook in rapporten en publicaties over het onderzoek zijn de gegevens niet tot u te herleiden.

Toegang tot uw gegevens voor controle

Sommige personen kunnen op de onderzoekslocatie toegang krijgen tot al uw gegevens. Ook tot de gegevens zonder code. Dit is nodig om te kunnen controleren of het onderzoek goed en betrouwbaar is uitgevoerd. Personen die ter controle inzage krijgen in uw gegevens zijn: een controleur/monitor die voor het Erasmus MC werkt of die door het Erasmus MC is ingehuurd en nationale toezichthoudende autoriteiten, bijvoorbeeld, de Inspectie Gezondheidszorg en Jeugd. Zij houden uw gegevens geheim. Wij vragen u voor deze inzage toestemming te geven.

Bewaartermijn gegevens en lichaamsmateriaal

Uw gegevens moeten 15 jaar na afloop van de studie worden bewaard op de onderzoekslocatie. Uw lichaamsmateriaal wordt niet onmiddellijk na gebruik vernietigd. Het wordt bewaard om daarop in de loop van dit onderzoek nog nieuwe bepalingen te kunnen doen die te maken hebben met dit onderzoek. Bewaren en gebruik van gegevens en lichaamsmateriaal voor ander onderzoek Uw gegevens en lichaamsmateriaal kunnen na afloop van dit onderzoek ook nog van belang zijn voor ander wetenschappelijk onderzoek op het gebied van eierstokkanker. Daarvoor zullen uw gegevens en lichaamsmateriaal 15 jaar worden bewaard. U kunt op het toestemmingsformulier aangeven of u hier wel of niet mee instemt. Indien u hier niet mee instemt, kunt u gewoon deelnemen aan het huidige onderzoek.

Intrekken toestemming

U kunt uw toestemming voor gebruik van uw persoonsgegevens altijd weer intrekken. Dit geldt voor dit onderzoek en ook voor het bewaren en het gebruik voor het toekomstige onderzoek. De onderzoeksgegevens die zijn verzameld tot het moment dat u uw toestemming intrekt worden nog wel gebruikt in het onderzoek. Uw lichaamsmateriaal wordt na intrekking van uw toestemming vernietigd. Als er al metingen met dat lichaamsmateriaal zijn gedaan, dan worden die gegevens nog wel gebruikt.

Voor het intrekken van uw toestemming is een intrekkingsformulier toegevoegd als laatste bijlage bij deze informatiebrief. U kunt dit formulier afgeven aan uw behandelend arts of verpleegkundige of opsturen naar

het Erasmus MC.

Meer informatie over uw rechten bij verwerking van gegevens Voor algemene informatie over uw rechten bij verwerking van uw persoonsgegevens kunt u de website van de Autoriteit Persoonsgegevens raadplegen. Bij vragen over uw rechten kunt u contact opnemen met de verantwoordelijke voor de verwerking van uw persoonsgegevens. Voor dit onderzoek is dat het Erasmus MC (zie bijlage A voor contactgegevens). Bij vragen of klachten over de verwerking van uw persoonsgegevens raden we u aan eerst contact op te nemen met de onderzoekslocatie. U kunt ook contact opnemen met de Functionaris voor de Gegevensbescherming van de instelling (zie bijlage A voor contactgegevens) of de Autoriteit Persoonsgegevens.

8. Zijn er extra kosten/is er een vergoeding wanneer u besluit aan dit onderzoek mee te doen?

Er zijn geen extra kosten en er is geen vergoeding bij deelname aan dit onderzoek.

9. Welke toetsingscommissie heeft dit onderzoek goedgekeurd?

De Medisch-Ethische Toetsingscommissie (METC) van het Erasmus MC heeft voor dit onderzoek een verklaring 'niet WMO-plichtig onderzoek' afgegeven. Dat betekent dat dit onderzoek door de onderzoeker is aangemeld bij deze METC en niet valt onder de wet medisch-wetenschappelijk onderzoek met mensen.

10. Heeft u vragen?

Bij vragen kunt u contact opnemen met het onderzoeksteam. Voor onafhankelijk advies over meedoen aan dit onderzoek kunt u terecht bij de onafhankelijke arts. Hij weet veel over het onderzoek, maar heeft niets te maken met dit onderzoek. Indien u klachten heeft over het onderzoek, kunt u dit bespreken met de onderzoeker of uw behandelend arts. Wilt u dit liever niet, dan kunt u zich wenden tot de klachtenfunctionaris of klachtencommissie van uw ziekenhuis. Alle gegevens vindt u in bijlage A: Contactgegevens.

11. Ondertekening toestemmingsformulier

Wanneer u voldoende bedenktijd heeft gehad, wordt u gevraagd te beslissen over deelname aan dit onderzoek. Indien u toestemming geeft, zullen wij u vragen deze op de bijbehorende toestemmingsverklaring schriftelijk te bevestigen. Door uw schriftelijke toestemming geeft u aan dat u de informatie heeft begrepen en instemt met deelname aan het onderzoek. Zowel uzelf als de onderzoeker ontvangen een getekende versie van deze toestemmingsverklaring.

Met vriendelijke groet,
namens het onderzoeksteam,
Dr. H.J. van Beekhuizen, gynaecoloog-oncoloog Erasmus MC
Dr. M. Jozwiak, gynaecoloog Erasmus MC
Dr. G.M. Nieuwenhuyzen, gynaecoloog-oncoloog Erasmus MC
Prof. Dr. J. Dankelman, Biomechanical engineering
S.M. Perez, Biomedical Engineering

12. Bijlagen

A: Contactgegevens Erasmus MC
B. Toestemmingsformulier proefpersoon
C: Formulier voor intrekken eerder verleende toestemming

Bijlage A: Contactgegevens Erasmus MC

Hoofdonderzoeker:
Drs. G.M. Nieuwenhuyzen, gynaecoloog-oncoloog
Bereikbaar via het secretariaat, tel. 010 – 703 33 81

Onderzoeksartsen:
Dr. H.J. van Beekhuizen, gynaecoloog-oncoloog
Dr. M. Józwiak, gynaecoloog
Bereikbaar via het secretariaat, tel. 010 – 703 33 81

Klachten:
De Klachtencommissie Erasmus MC is bereikbaar via tel. 010 – 703 31 98 of e-mail klachtenopvang@erasmusmc.nl.

Functionaris voor de Gegevensbescherming van de instelling:
De Functionaris voor de Gegevensbescherming van het Erasmus MC is bereikbaar via het secretariaat van de afdeling Juridische Zaken, tel. 010- 703 49 86 of e-mail gegevensbescherming@erasmusmc.nl.

Voor meer informatie over uw rechten:
Voor meer informatie of bij vragen over uw rechten kunt u contact opnemen met de Functionaris voor de Gegevensbescherming of met de Autoriteit Persoonsgegevens.

Bijlage B: Toestemmingsformulier proefpersoon

Gebruik van weefsel van patiënten ten behoeven van het ontwikkelen van een manier voor het beter afbeelden van eierstokkanker bij operaties

- Ik heb de informatiebrief gelezen. Ook kon ik vragen stellen. Mijn vragen zijn voldoende beantwoord. Ik had genoeg tijd om te beslissen of ik meedoe.
- Ik weet dat meedoen vrijwillig is. Ook weet ik dat ik op ieder moment kan beslissen om toch niet mee te doen of te stoppen met het onderzoek. Daarvoor hoef ik geen reden te geven.
- Ik geef toestemming voor het opvragen van informatie bij mijn huisarts/specialist(en) die mij behandelt.
- Ik geef toestemming voor het verzamelen en gebruiken van mijn gegevens en lichaamsmateriaal voor de beantwoording van de onderzoeksvraag in dit onderzoek.
- Ik weet dat voor de controle van het onderzoek sommige mensen toegang tot al mijn gegevens kunnen krijgen. Die mensen staan vermeld in deze informatiebrief. Ik geef toestemming voor die inzage door deze personen.
- Ik geef O wel O geen
  toestemming om mijn persoonsgegevens langer te bewaren en te gebruiken voor toekomstig onderzoek op het gebied van eierstokkanker.
- Ik geef O wel O geen
  toestemming om mijn lichaamsmateriaal na dit onderzoek te bewaren en om dit later nog voor ander/meer onderzoek te gebruiken, zoals in de informatiebrief staat.
- Ik geef O wel O geen
  toestemming om mij na dit onderzoek opnieuw te benaderen voor een vervolgonderzoek.
- Ik wil meedoen aan dit onderzoek.

Naam proefpersoon:
Handtekening:
Datum:

Ik verklaar dat ik deze proefpersoon volledig heb geïnformeerd over het genoemde onderzoek. Als er tijdens het onderzoek informatie bekend wordt die de toestemming van de proefpersoon zou kunnen beïnvloeden, dan breng ik hem/haar daarvan tijdig op de hoogte.

Naam onderzoeker (of diens vertegenwoordiger):
Handtekening:
Datum:

<indien van toepassing>
Aanvullende informatie is gegeven door:
Naam:
Functie:
Handtekening:
Datum:

De proefpersoon krijgt een volledige informatiebrief mee, samen met een getekende versie van het toestemmingsformulier.

Bijlage C: Formulier voor intrekken eerder verleende toestemming

Gebruik van weefsel van patiënten ten behoeven van het ontwikkelen van een manier voor het beter afbeelden van eierstokkanker bij operaties

Ik geef hiermee te kennen dat ik mijn deelname aan de studie intrek. Dit betekent dat van mij geen medische gegevens meer mogen worden verzameld voor gebruik binnen de studie.

Ik begrijp dat lichaamsmateriaal dat bij mij is afgenomen en al in een onderzoek is bewerkt, niet wordt teruggehaald of wordt vernietigd. Voorts ben ik mij bewust dat de medische gegevens die in een onderzoek zijn gebruikt niet worden teruggehaald of vernietigd. Dit lichaamsmateriaal en deze medische gegevens blijven gecodeerd ter beschikking van degene die het onderzoek uitvoert.

Over het van mij nog opgeslagen lichaamsmateriaal ten behoeve van de studie verklaar ik dat mijn lichaamsmateriaal:

O nog steeds gebruikt mag worden volgens het door mij eerder ondertekende toestemmingsformulier;

O vernietigd moet worden.

Naam:
Geboortedatum:
Datum:
Handtekening:

Formulier opsturen naar:
Drs. G.M. Nieuwenhuyzen (hoofdonderzoeker)
Afdeling Gynaecologische Oncologie
Erasmus MC
Antwoordnummer 55
3000 WB Rotterdam

Ik verklaar kennis genomen te hebben van het intrekken van de toestemming door de bovenvermelde patiënt en zoals hierboven omschreven.

Naam:
Datum:
Handtekening:

C

Appendix: Code

Calibration

A python algorithm was used to calibrate the HSI, sort the hypercube from lowest wavelength to highest wavelength and convert the HS cube from *.pgm format to *.mat struct.

\lstinputlisting{calibration.py}

Normalisation

Thereafter the image was preprocessed by min-max normalisation

```
function [p_training,p_label]=acquisition(p_HSI_or,p_RGB,p_PA_or,fixedPoints_p_HSI,
    movingPoints_p_HSI,fixedPoints_p_PA,movingPoints_p_PA)
p_HSI_norm = [];
    for k = 1:size(p_HSI_or,3)
        %Load image
        image_p=p_HSI_or(:,:,k);
        %Scaling: SD [0,1] (min-max normalisation)
        image_norm=(image_p-min(min(image_p)))./(max(max(image_p))-min(min(image_p))
            );
        %Collection of the hypercube
        p_HSI_norm = cat(3,p_HSI_norm, image_norm);
    end
```

Transformation

In order to be able to match the HSI with the pathological ground both the HSI image and PA image were transformed with the cp select tool within Matlab. Around 20 control points were selected.

```
% Affine control points based transofrmation HSI (moving) and PA (moving) on RGB (
    fixed) with function cpselect(moving, fixed).
%cpselect(p_HSI_or(:,:,1),p_RGB)
%cpselect(p_PA_or,p_RGB)
%affine transformation
tform_HSI = fitgeotrans(movingPoints_p_HSI,fixedPoints_p_HSI,'affine');
tform_PA = fitgeotrans(movingPoints_p_PA,fixedPoints_p_PA,'affine');

%HS and patholgical registered
p_HSI_adapted=[];
    for k = 1:size(p_HSI_or,3)
        movingRegistered_HSI = imwarp(p_HSI_norm(:,:,k),tform_HSI,'OutputView',
            imref2d(size(p_RGB)));
```

```
        p_HSI_adapted= cat(3,p_HSI_adapted, movingRegistered_HSI);
    end
p_PA_adapted=imwarp(p_PA_or,tform_PA,'OutputView',imref2d(size(p_RGB)));
```

Noise filtering

Noise was filtering by HSV thresholding.

```
%%Mask no noise
image = p_HSI_adapted;
% Define thresholds for 'Hue'. Modify these values to filter out different range of
    colors.
channel1Min_a = 0.140;
channel1Max_a = 0.800;
% Define thresholds for 'Saturation'
channel2Min_a = 0.210;
channel2Max_a = 0.800;
% Define thresholds for 'Value'
channel3Min_a = 0.140;
channel3Max_a = 0.800;
% Create mask based on chosen histogram thresholds
p_a_mask= ( (image(:,:,1) >= channel1Min_a) | (image(:,:,1) <= channel1Max_a) ) &
    ...
    (image(:,:,1) >= channel2Min_a ) & (image(:,:,1) <= channel2Max_a) & ...
    (image(:,:,1) >= channel3Min_a ) & (image(:,:,1) <= channel3Max_a);

%Create dataset healthy and tumour tissue
p_HSI_nn=[];
    for k = 1:size(p_HSI_adapted,3)
        HSI_nn=p_HSI_adapted(:,:,k).*p_a_mask;
        p_HSI_nn=cat(3,p_HSI_nn, HSI_nn);
    end
```

Segmentation

```
%Mask tumour tissue
image = rgb2hsv(p_PA_adapted);
% Define thresholds for 'Hue'. Modify these values to filter out different range of
    colors.
channel1Min_t = 0.347;
channel1Max_t = 0.348;
% Define thresholds for 'Saturation'
channel2Min_t = 0.815;
channel2Max_t = 0.820;
% Define thresholds for 'Value'
channel3Min_t = 0.360;
channel3Max_t = 0.369;
% Create mask based on chosen histogram thresholds
p_t_mask= ( (image(:,:,1) >= channel1Min_t) | (image(:,:,1) <= channel1Max_t) ) &
    ...
    (image(:,:,2) >= channel2Min_t ) & (image(:,:,2) <= channel2Max_t) & ...
    (image(:,:,3) >= channel3Min_t ) & (image(:,:,3) <= channel3Max_t);

%Mask healthy tissue
% Define thresholds for 'Hue'. Modify these values to filter out different range of
    colors.
```

```
channel1Min_h = 0.192;
channel1Max_h = 0.194;
% Define thresholds for 'Saturation'
channel2Min_h = 0.999;
channel2Max_h = 1.000;
% Define thresholds for 'Value'
channel3Min_h = 0.839;
channel3Max_h = 0.841;
% Create mask based on chosen histogram thresholds
p_h_mask= ( (image(:,:,1) >= channel1Min_h) | (image(:,:,1) <= channel1Max_h) ) &
    ...
    (image(:,:,2) >= channel2Min_h ) & (image(:,:,2) <= channel2Max_h) & ...
    (image(:,:,3) >= channel3Min_h ) & (image(:,:,3) <= channel3Max_h);

%Create dataset healthy and tumour tissue
p_HSI_t=[];
p_HSI_h=[];
    for k = 1:size(p_HSI_nn,3)
        HSI_t=p_HSI_nn(:,:,k).*p_t_mask;
        HSI_h=p_HSI_nn(:,:,k).*p_h_mask;
        p_HSI_t=cat(3,p_HSI_t, HSI_t);
        p_HSI_h=cat(3,p_HSI_h, HSI_h);
    end
```

Generation of patches

```
fun=@(theBlockStructure) mean(double(theBlockStructure.data(:)));
p_HSI_tb=[];
p_HSI_hb=[];
    for k=1:size (p_HSI_t,3)
        block_t=blockproc(p_HSI_t(:,:,k), [20 20],fun);
        block_h=blockproc(p_HSI_h(:,:,k), [20 20],fun);
        p_HSI_tb=cat(3,p_HSI_tb, block_t);
        p_HSI_hb=cat(3,p_HSI_hb, block_h);
    end
```

Formation of training set

```
% Create training set and label for tumour tissue
p_intensity_t = reshape(p_HSI_tb, (size(p_HSI_tb,1)*size(p_HSI_tb,2)),size(p_HSI_tb
    ,3));
p_intensity_t(all(~p_intensity_t,2),:)=[]; %remove rows of 0
label_t=ones(size(p_intensity_t,1),1);

% Create training set and label for healthy tissue
p_intensity_h = reshape(p_HSI_hb, (size(p_HSI_hb,1)*size(p_HSI_hb,2)),size(p_HSI_hb
    ,3));
p_intensity_h(all(~p_intensity_h,2),:)=[]; %remove rows of 0
label_h=ones(size(p_intensity_h,1),1).*2;

% Make training dataset
p_intensity=[p_intensity_t;p_intensity_h];
p_der=(diff(p_intensity'))';
p_norm1=p_intensity./p_intensity(:,1);
p_norm2=p_intensity./p_intensity(:,2);
p_norm3=p_intensity./p_intensity(:,3);
p_norm4=p_intensity./p_intensity(:,4);
```

```
p_norm5=p_intensity./p_intensity(:,5);
p_norm6=p_intensity./p_intensity(:,6);
p_norm7=p_intensity./p_intensity(:,7);
p_norm8=p_intensity./p_intensity(:,8);
p_norm9=p_intensity./p_intensity(:,9);
p_norm10=p_intensity./p_intensity(:,10);
p_norm11=p_intensity./p_intensity(:,11);
p_norm12=p_intensity./p_intensity(:,12);
p_norm13=p_intensity./p_intensity(:,13);
p_norm14=p_intensity./p_intensity(:,14);
p_norm15=p_intensity./p_intensity(:,15);
p_norm16=p_intensity./p_intensity(:,16);
p_norm17=p_intensity./p_intensity(:,17);
p_norm18=p_intensity./p_intensity(:,18);
p_norm19=p_intensity./p_intensity(:,19);
p_norm20=p_intensity./p_intensity(:,20);
p_norm21=p_intensity./p_intensity(:,21);
p_norm22=p_intensity./p_intensity(:,22);
p_norm23=p_intensity./p_intensity(:,23);
p_norm24=p_intensity./p_intensity(:,24);
p_norm25=p_intensity./p_intensity(:,25);
%p_avg=mean(p_intensity,2);
%p_k=(kurtosis(p_intensity'))';

%p_training=[p_intensity,p_der,p_norm1,p_norm2,p_norm3,p_norm4,p_norm5,p_norm6,
    p_norm7,p_norm8,p_norm9,p_norm10,p_norm11,p_norm12,p_norm13,p_norm14,p_norm15,
    p_norm16,p_norm17,p_norm18,p_norm19,p_norm20,p_norm21,p_norm22,p_norm23,p_norm24,
    p_norm25];
p_training= [p_der(:,[2 17 21 24]),p_intensity(:,[3 8 10 12 15 16 19 20 21]),
    p_norm20(:,[1 3 7 16 21 22])];
p_label=[label_t;label_h];
end
```

SVM classifier

```
function [fpr,tpr,auc,TP,FN,FP,TN,spec,sen,PPV,NPV,MCC]=SVM(training_set,
    training_label,test_set,test_label)
t=sum(training_label==1);
h=sum(training_label==2);
w=[ones(t,1);ones(h,1)*(t/h)];


%Classification models
SVM_model = fitcsvm(training_set,training_label,'KernelFunction','linear','Weights',
    w);
RBFSVM_model = fitcsvm(training_set,training_label,'KernelFunction','rbf','
    ClassNames','Weights',w);
kNN_model = fitcknn(training_set,training_label,'NumNeighbors',66,'Weights',w);

[label,score] =predict(SVM_model,test_set);
[fpr,tpr,T,auc] = perfcurve(test_label,score(:,1),1);

%Youden statistic
sen=tpr;
spec=1-fpr;
j=sen+spec-1;
[~,B]=max(j);
```

```
20
21 %Performance
22 [TP_all,FN_all] = perfcurve(test_label,score(:,1),1,'XCrit','tp','yCrit','fn');
23 [FP_all,TN_all] = perfcurve(test_label,score(:,1),1,'XCrit','fp','yCrit','tn');
24 TP=TP_all(B,1);
25 FN=FN_all(B,1);
26 FP=FP_all(B,1);
27 TN=TN_all(B,1);
28
29 spec=TN/(TN+FP);
30 sen=TP/(TP+FN);
31 PPV=TP/(TP+FP);
32 NPV=TN/(TN+FN);
33 MCC=((TP*TN)-(FP*FN))/sqrt((TP+FP)*(TP+FN)*(TN+FP)*(TN+FN));
34
35 end
```

D

Appendix: Results Matlab

Patient 1 tissue A

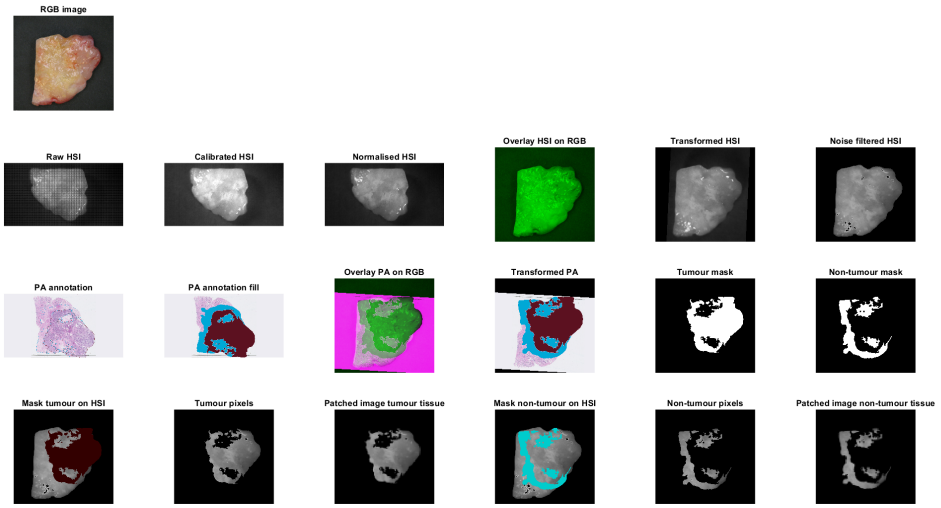

Figure D.1: Patient 1 tissue A

Patient 1 tissue B

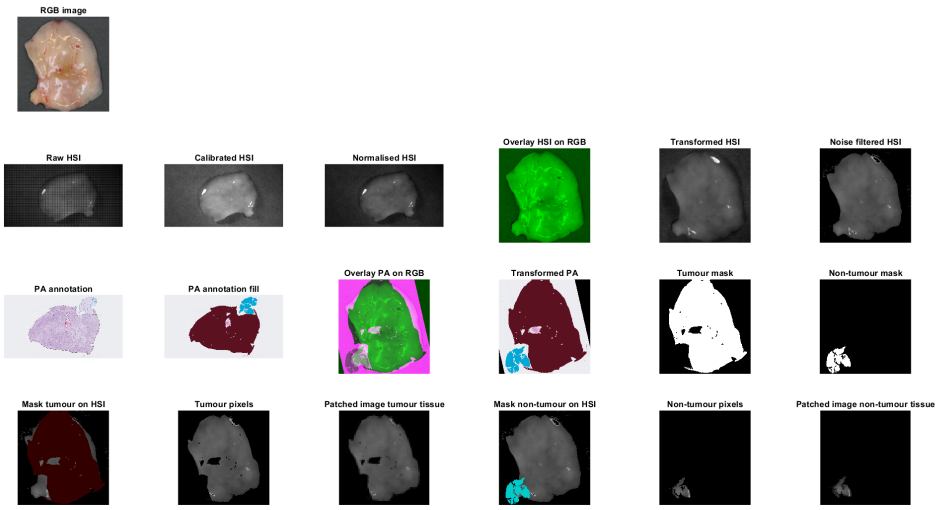

Figure D.2: Patient 1 tissue B

Patient 1 tissue C

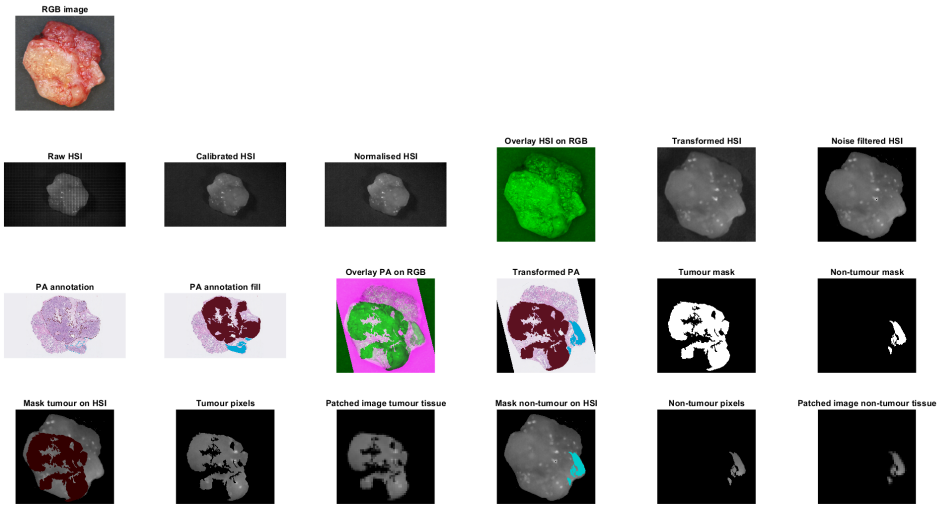

Figure D.3: Patient 1 tissue C

Patient 1 tissue D

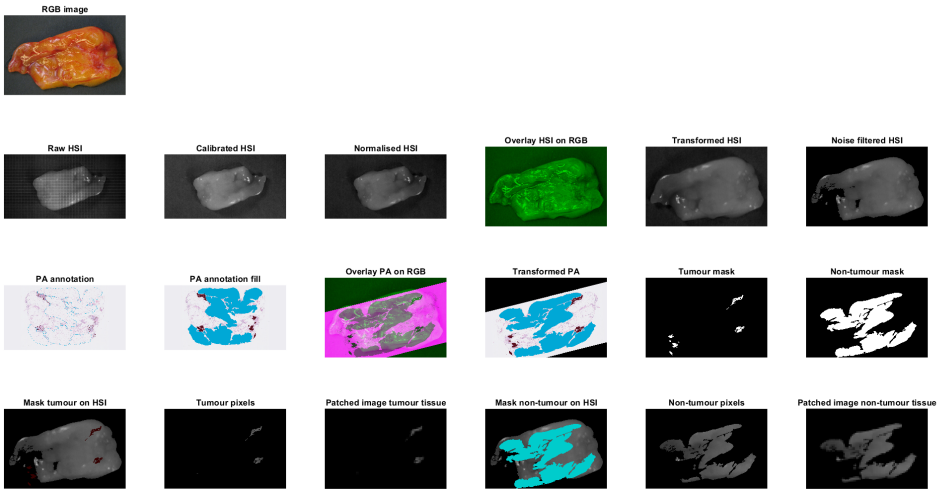

Figure D.4: Patient 1 tissue D

Patient 2 tissue A

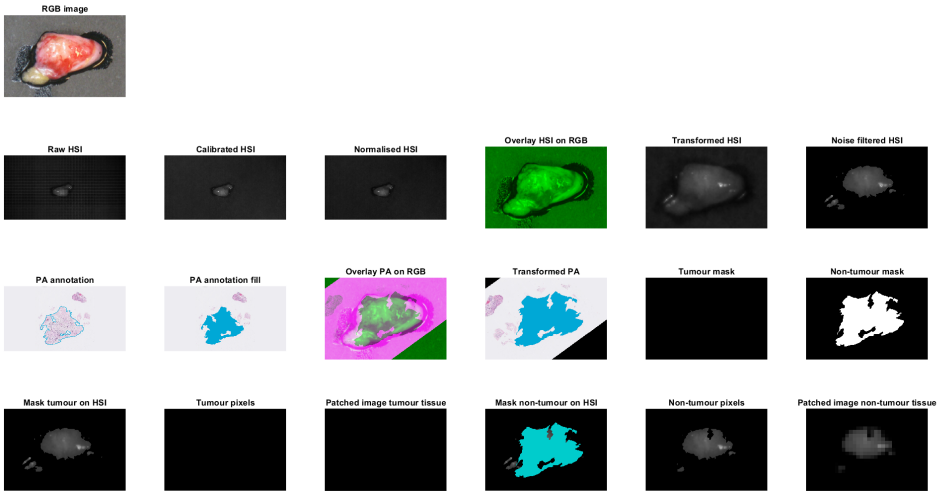

Figure D.5: Patient 2 tissue A

Patient 3 tissue A

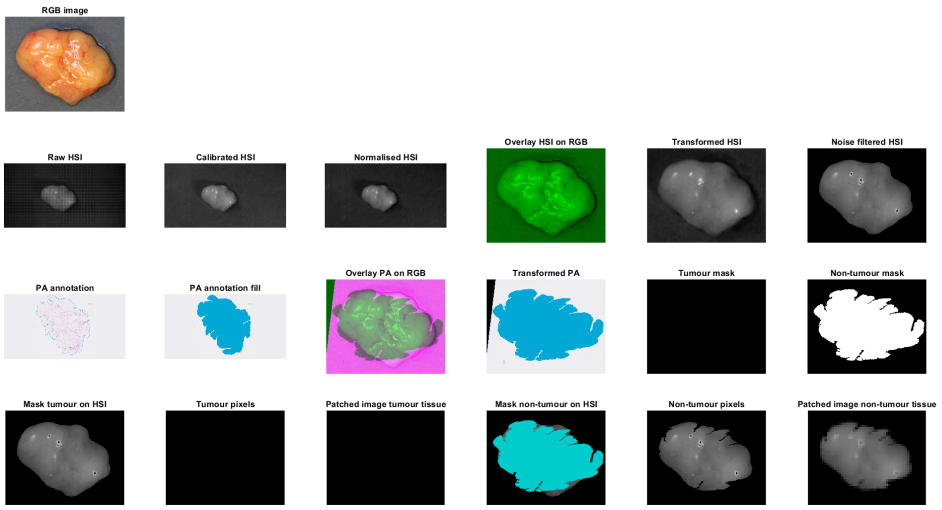

Figure D.6: Patient 3 tissue A

Patient 3 tissue B

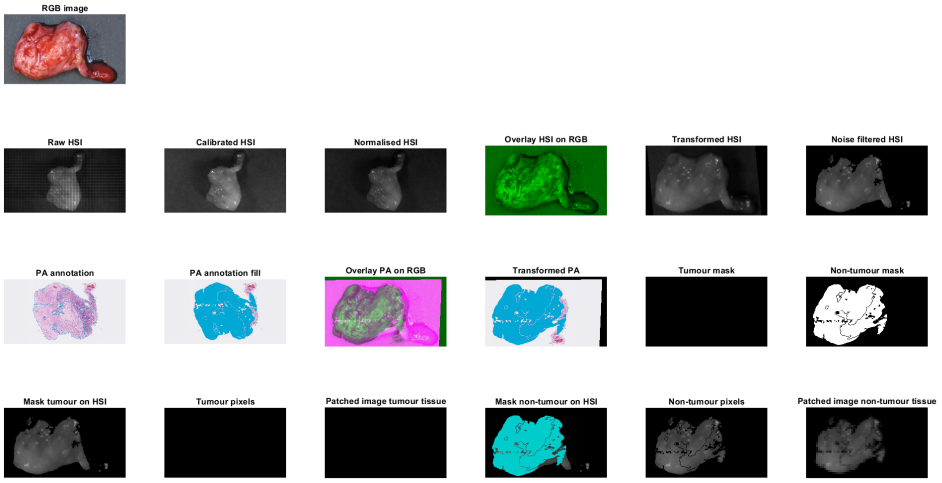

Figure D.7: Patient 3 tissue B

Patient 4 tissue A

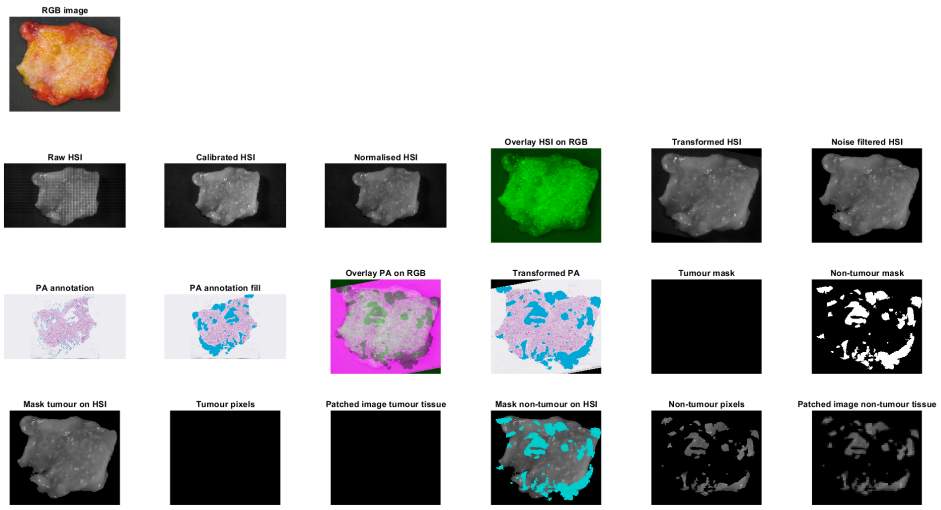

Figure D.8: Patient 4 tissue A

Patient 4 tissue B

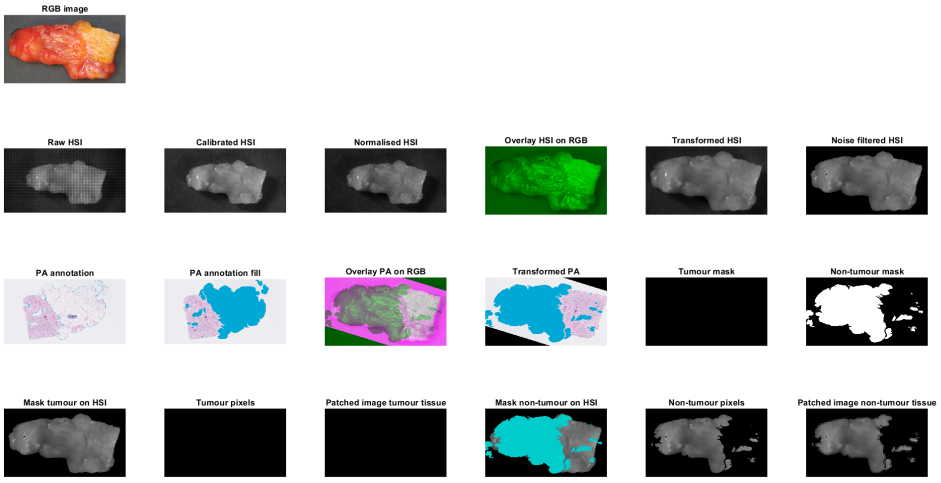

Figure D.9: Patient 4 tissue B

Patient 4 tissue C

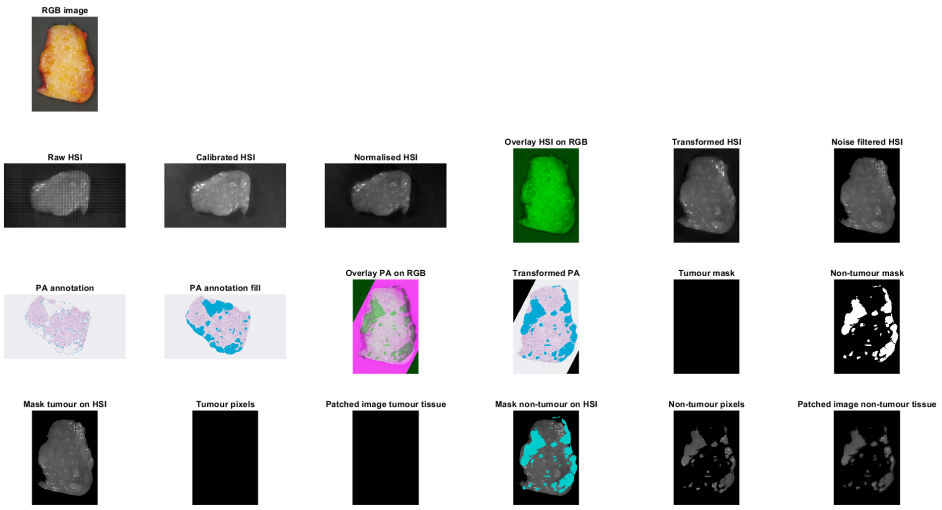

Figure D.10: Patient 4 tissue C

Patient 6 tissue A

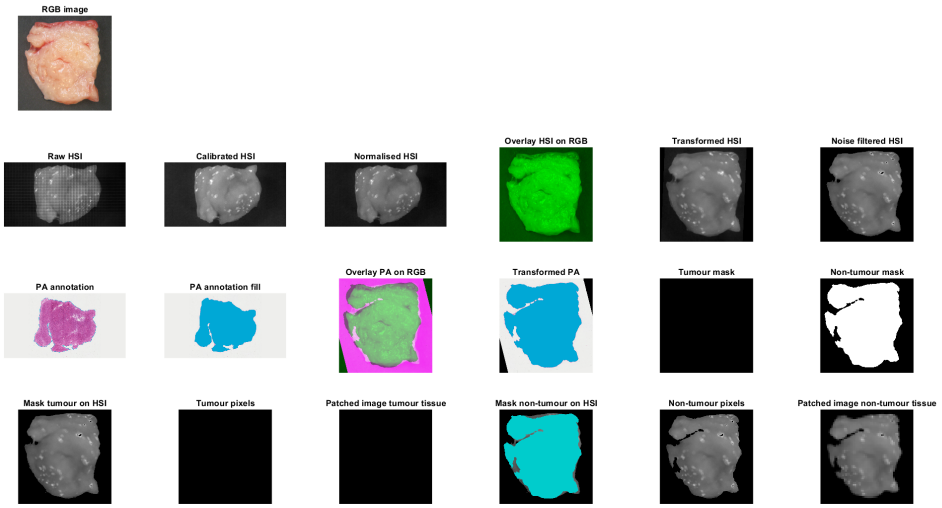

Figure D.11: Patient 6 tissue A

Patient 6 tissue B

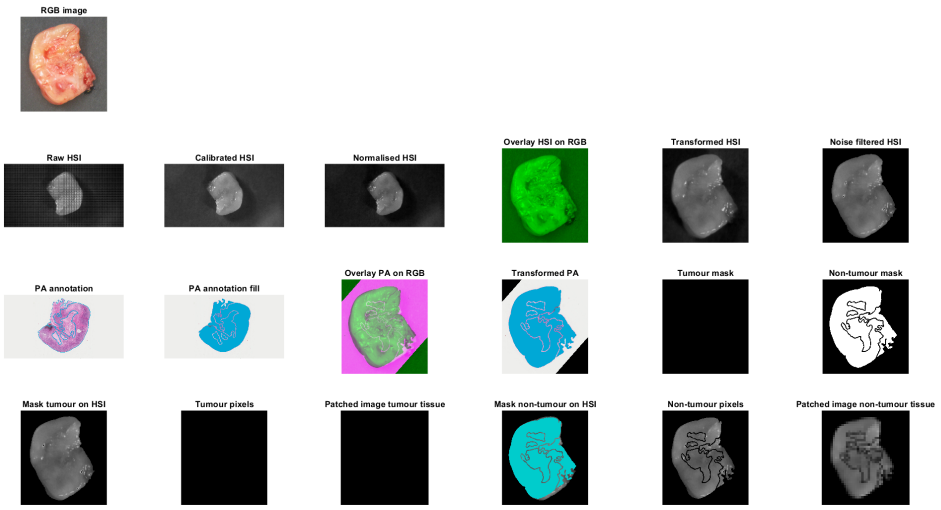

Figure D.12: Patient 6 tissue B

Patient 6 tissue C

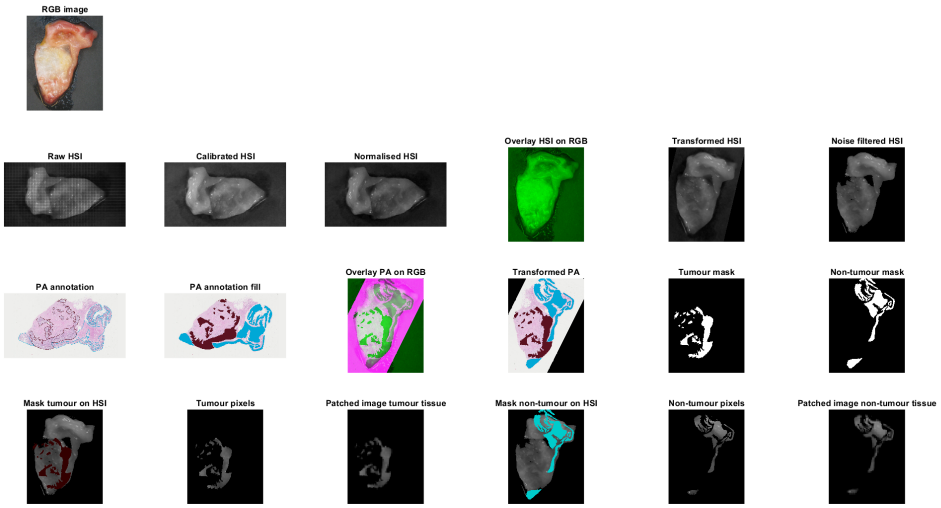

Figure D.13: Patient 6 tissue C

Patient 6 tissue D

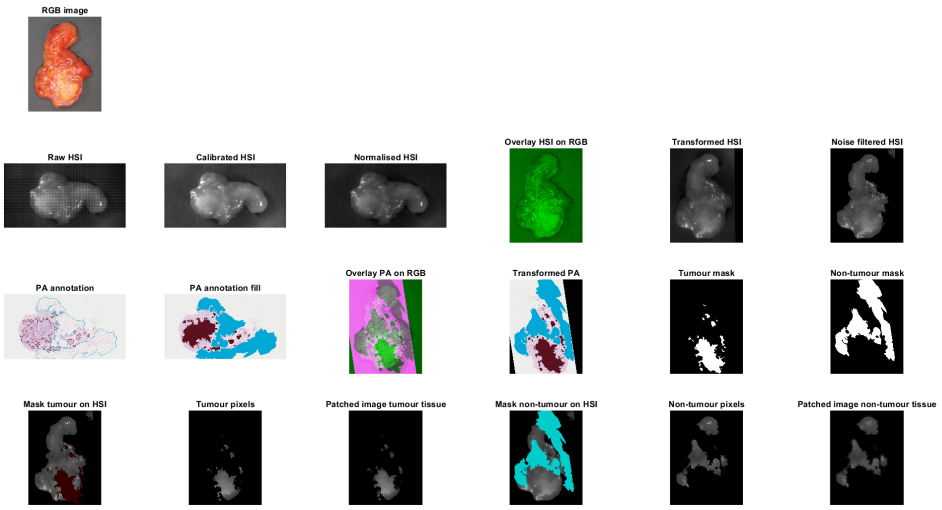

Figure D.14: Patient 6 tissue D

Patient 6 tissue E

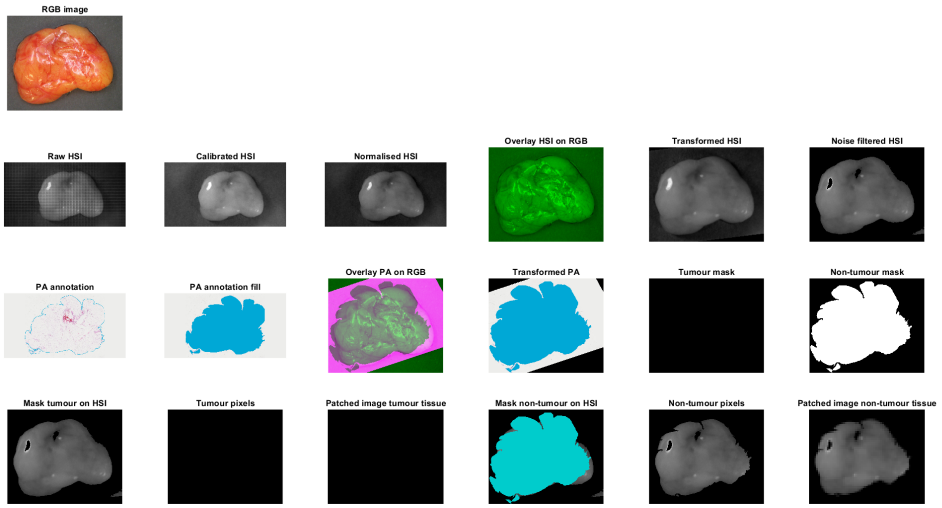

Figure D.15: Patient 6 tissue E

Patient 7 tissue A

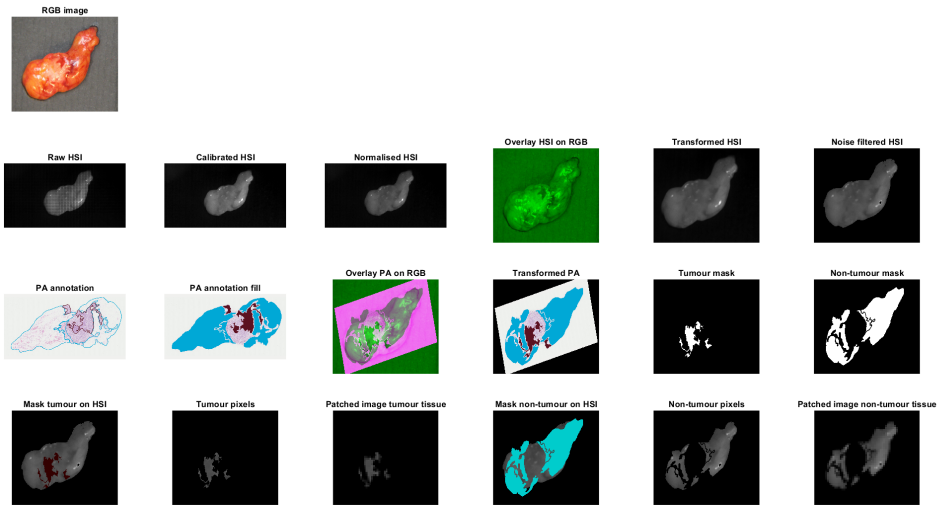

Figure D.16: Patient 7 tissue A

Patient 7 tissue B

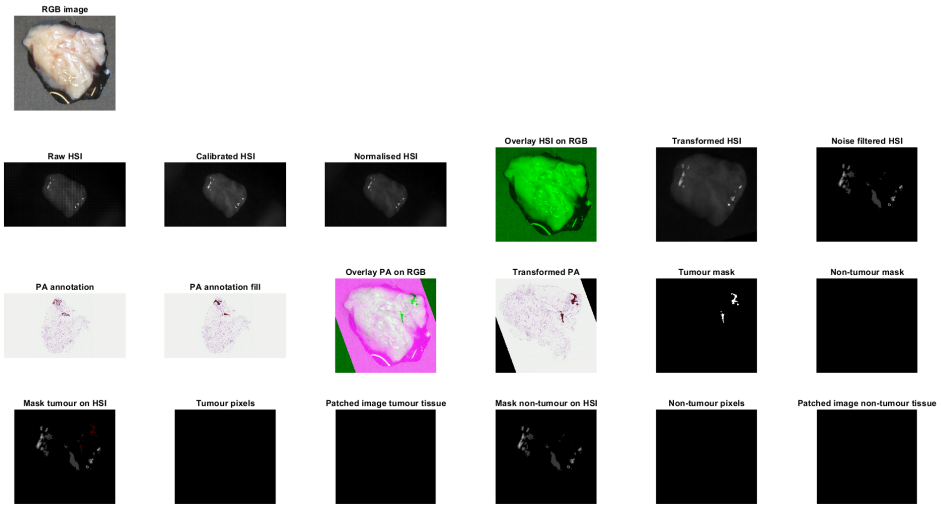

Figure D.17: Patient 7 tissue B

Patient 7 tissue C

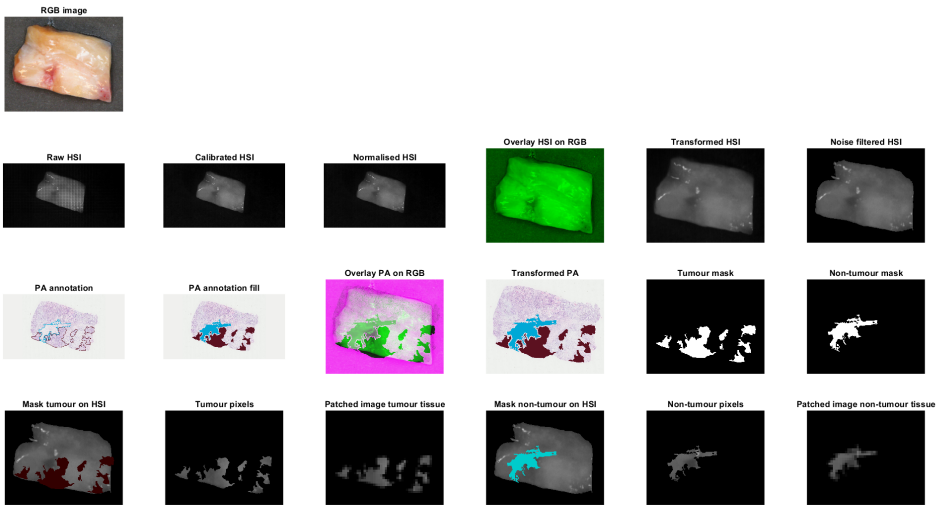

Figure D.18: Patient 7 tissue C

Patient 8 tissue A

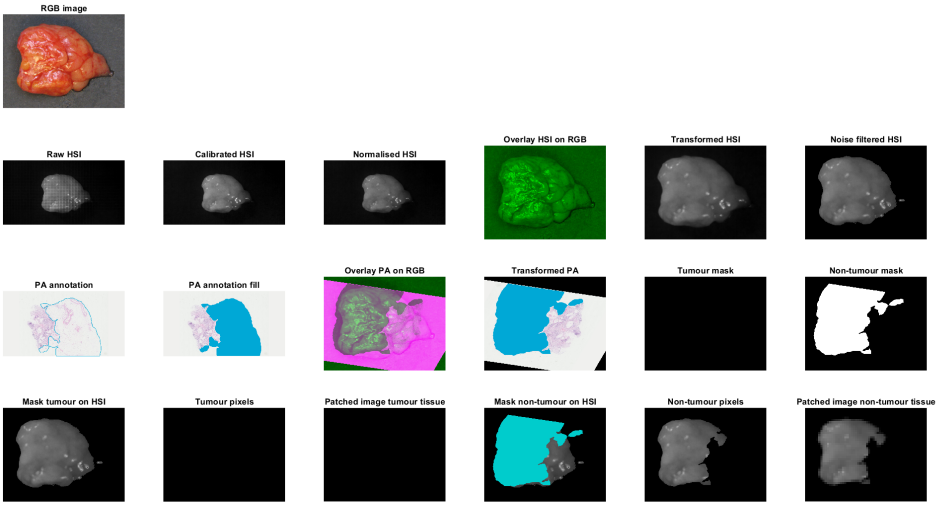

Figure D.19: Patient 8 tissue A

Patient 8 tissue B

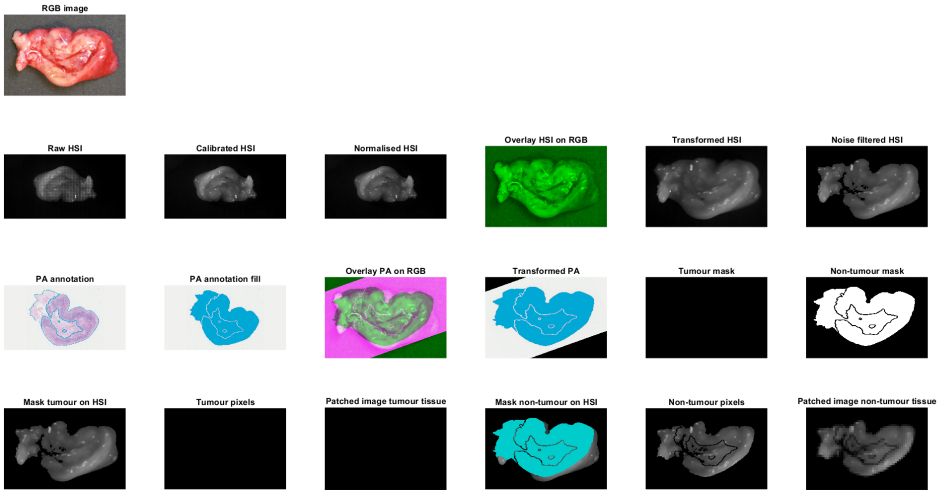

Figure D.20: Patient 8 tissue B

Patient 9 tissue A

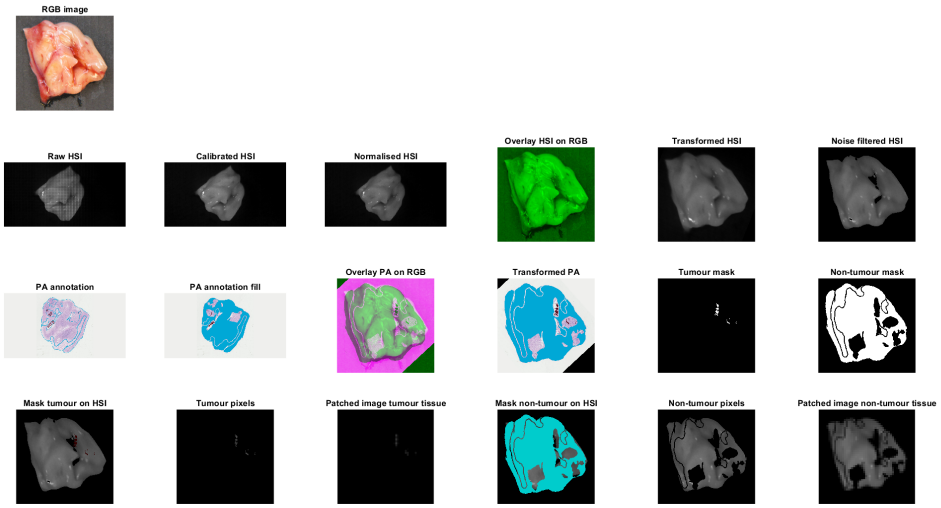

Figure D.21: Patient 9 tissue A

Patient 9 tissue B

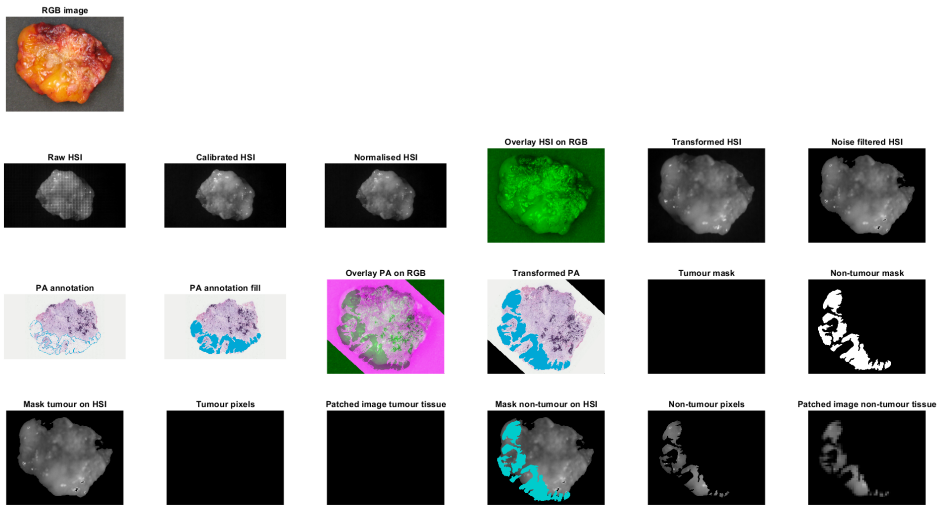

Figure D.22: Patient 9 tissue B

Patient 10 tissue A

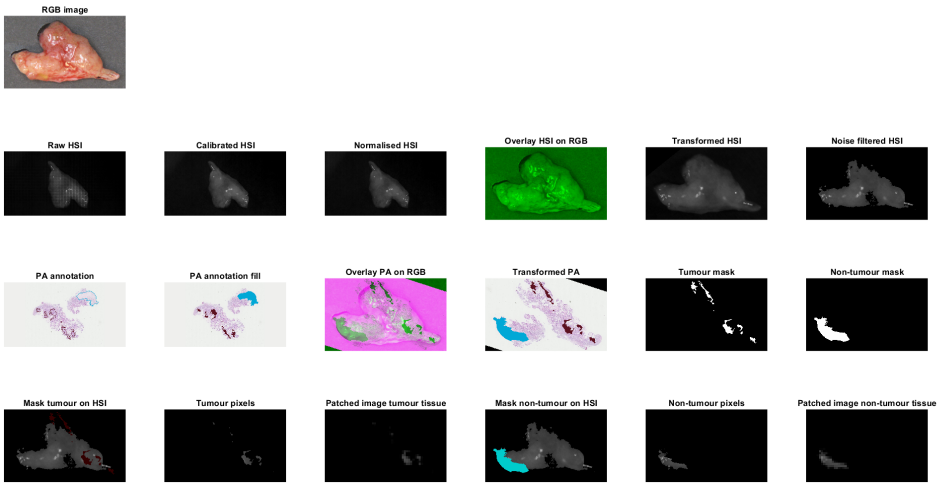

Figure D.23: Patient 10 tissue A

Patient 10 tissue B

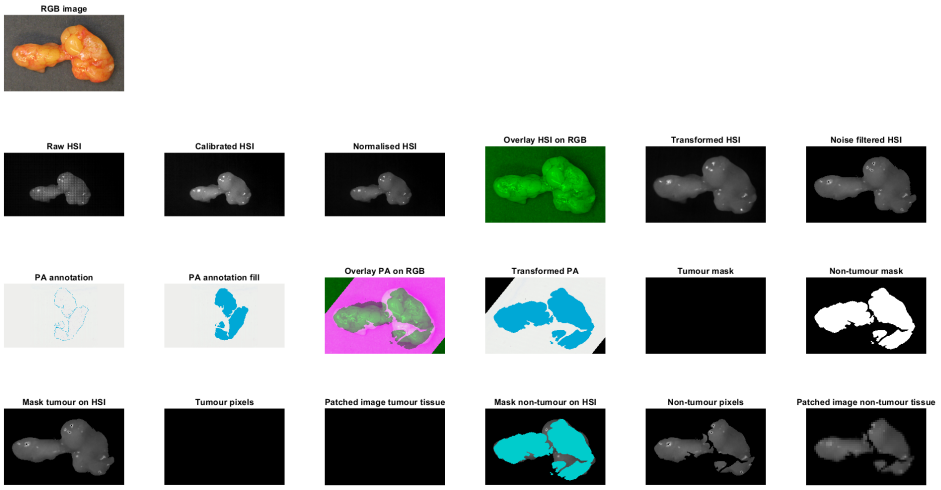

Figure D.24: Patient 10 tissue B

Patient 10 tissue C

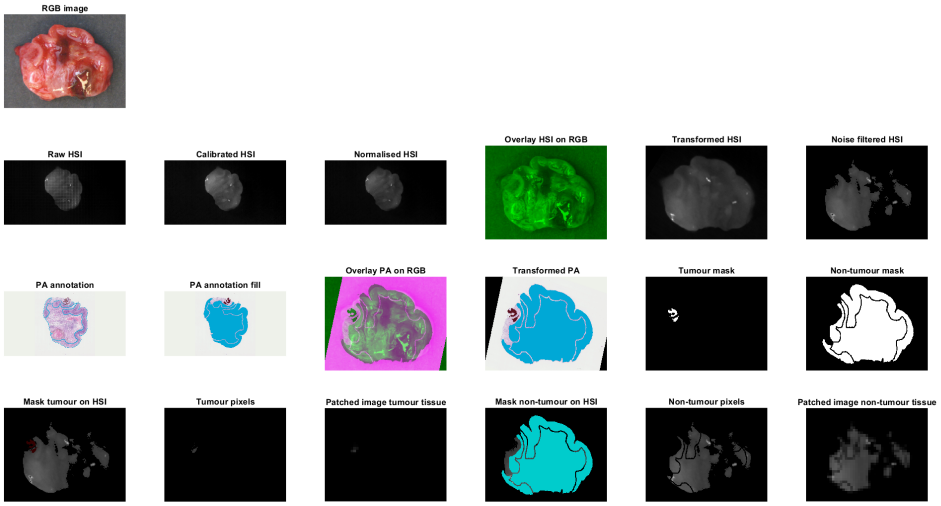

Figure D.25: Patient 10 tissue C

Patient 11 tissue A

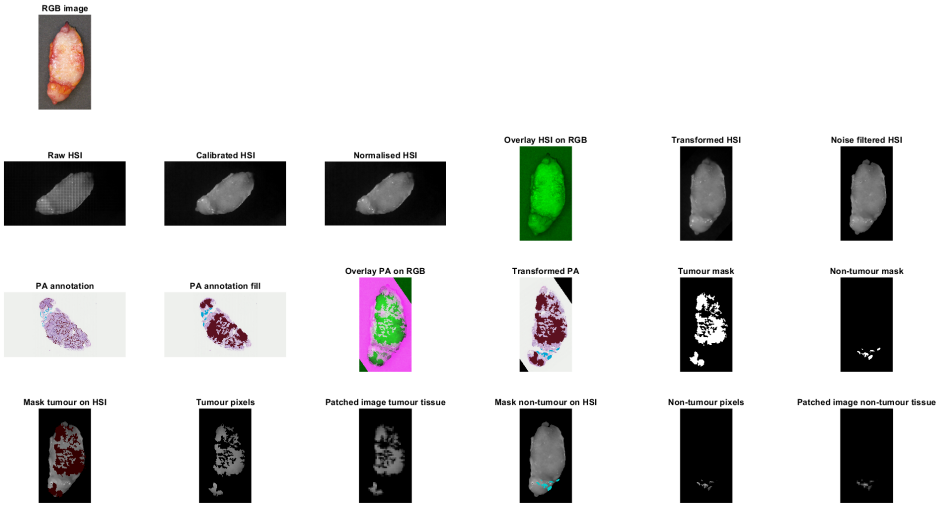

Figure D.26: Patient 11 tissue A

E

Appendix: Feature selection

Table E.1: P-score of features

WL [nm]	Int	Der	Norm676	Norm684	Norm679	Norm711	Norm735	Norm749	Norm762
676	<0.001	<0.001	-	<0.001	<0.001	<0.001	<0.001	0.087	<0.001
684	<0.001	<0.001	<0.001	-	<0.001	<0.001	<0.001	<0.001	<0.001
697	<0.001	<0.001	<0.001	<0.001	-	<0.001	0.022	<0.001	<0.001
711	<0.001	<0.001	<0.001	<0.001	<0.001	-	<0.001	<0.001	<0.001
735	<0.001	<0.001	<0.001	<0.001	<0.001	<0.001	-	<0.001	<0.001
749	<0.001	<0.001	<0.001	<0.001	<0.001	<0.001	<0.001	-	<0.001
762	<0.001	<0.001	<0.001	<0.001	<0.001	<0.001	<0.001	<0.001	-
775	<0.001	<0.001	<0.001	<0.001	<0.001	<0.001	<0.001	<0.001	<0.001
786	0.066	<0.001	<0.001	<0.001	<0.001	<0.001	<0.001	<0.001	<0.001
799	<0.001	<0.001	<0.001	<0.001	<0.001	<0.001	<0.001	<0.001	<0.001
811	<0.001	<0.001	<0.001	<0.001	<0.001	<0.001	<0.001	<0.001	<0.001
823	<0.001	<0.001	<0.001	<0.001	<0.001	<0.001	<0.001	<0.001	<0.001
841	<0.001	<0.001	<0.001	<0.001	<0.001	<0.001	<0.001	<0.001	<0.001
852	<0.001	<0.001	<0.001	<0.001	<0.001	<0.001	<0.001	<0.001	<0.001
863	<0.001	<0.001	<0.001	<0.001	<0.001	<0.001	<0.001	<0.001	<0.001
872	<0.001	<0.001	<0.001	<0.001	<0.001	<0.001	<0.001	<0.001	<0.001
882	<0.001	<0.001	<0.001	<0.001	<0.001	<0.001	<0.001	<0.001	<0.001
892	0.001	<0.001	<0.001	<0.001	<0.001	<0.001	<0.001	<0.001	<0.001
901	<0.001	<0.001	<0.001	<0.001	<0.001	<0.001	<0.001	<0.001	<0.001
910	<0.001	<0.001	<0.001	<0.001	<0.001	<0.001	<0.001	<0.001	<0.001
923	<0.001	<0.001	<0.001	<0.001	<0.001	<0.001	<0.001	<0.001	<0.001
930	0.621	<0.001	<0.001	<0.001	<0.001	<0.001	<0.001	<0.001	<0.001
938	<0.001	<0.001	<0.001	<0.001	<0.001	<0.001	<0.001	0.009	<0.001
943	0.356	<0.001	<0.001	<0.001	<0.001	<0.001	<0.001	<0.001	<0.001
954	<0.001	-	<0.001	<0.001	<0.001	<0.001	<0.001	<0.001	0.028

Table E.2: P-score of features

Wavelength	Norm8	Norm9	Norm10	Norm11	Norm12	Norm13	Norm14	Norm15	Norm16
676	<0.001	<0.001	<0.001	<0.001	<0.001	<0.001	<0.001	<0.001	<0.001
684	0.002	<0.001	<0.001	<0.001	<0.001	<0.001	<0.001	<0.001	<0.001
697	<0.001	<0.001	<0.001	<0.001	<0.001	<0.001	<0.001	<0.001	<0.001
711	<0.001	<0.001	<0.001	<0.001	<0.001	<0.001	<0.001	<0.001	<0.001
735	<0.001	<0.001	<0.001	<0.001	<0.001	<0.001	<0.001	<0.001	<0.001
749	<0.001	<0.001	<0.001	<0.001	<0.001	<0.001	<0.001	<0.001	<0.001
762	<0.001	<0.001	<0.001	<0.001	<0.001	<0.001	<0.001	<0.001	<0.001
775	-	<0.001	<0.001	<0.001	<0.001	<0.001	<0.001	<0.001	<0.001
786	<0.001	-	<0.001	<0.001	<0.001	<0.001	<0.001	<0.001	<0.001
799	<0.001	<0.001	-	<0.001	0.007	<0.001	<0.001	<0.001	<0.001
811	<0.001	<0.001	<0.001	-	<0.001	<0.001	<0.001	<0.001	<0.001
823	<0.001	<0.001	0.408	<0.001	-	<0.001	<0.001	<0.001	<0.001
841	<0.001	<0.001	<0.001	<0.001	<0.001	-	<0.001	<0.001	<0.001
852	<0.001	<0.001	<0.001	<0.001	<0.001	<0.001	-	<0.001	<0.001
863	<0.001	<0.001	<0.001	<0.001	<0.001	<0.001	<0.001	-	<0.001
872	<0.001	<0.001	<0.001	<0.001	<0.001	<0.001	<0.001	<0.001	-
882	<0.001	<0.001	<0.001	<0.001	<0.001	<0.001	<0.001	<0.001	<0.001
892	<0.001	<0.001	<0.001	<0.001	<0.001	<0.001	<0.001	<0.001	<0.001
901	<0.001	<0.001	<0.001	<0.001	<0.001	<0.001	0.309	<0.001	<0.001
910	<0.001	<0.001	<0.001	0.041	<0.001	<0.001	<0.001	<0.001	<0.001
923	<0.001	<0.001	<0.001	<0.001	<0.001	<0.001	<0.001	<0.001	<0.001
930	<0.001	<0.001	<0.001	<0.001	<0.001	<0.001	<0.001	<0.001	<0.001
938	<0.001	<0.001	<0.001	<0.001	<0.001	0.099	<0.001	<0.001	<0.001
943	<0.001	<0.001	<0.001	<0.001	<0.001	<0.001	<0.001	<0.001	<0.001
954	<0.001	<0.001	<0.001	<0.001	<0.001	<0.001	<0.001	<0.001	<0.001

Table E.3: P-score of features

Wavelength	Norm17	Norm18	Norm19	Norm20	Norm21	Norm22	Norm23	Norm24	Norm25
676	<0.001	<0.001	<0.001	<0.001	<0.001	<0.001	<0.001	<0.001	<0.001
684	<0.001	<0.001	<0.001	<0.001	<0.001	<0.001	<0.001	<0.001	<0.001
697	<0.001	<0.001	<0.001	<0.001	<0.001	<0.001	<0.001	<0.001	<0.001
711	<0.001	<0.001	<0.001	<0.001	<0.001	<0.001	<0.001	<0.001	<0.001
735	<0.001	<0.001	<0.001	<0.001	<0.001	<0.001	<0.001	<0.001	<0.001
749	<0.001	<0.001	<0.001	<0.001	<0.001	<0.001	0.051	<0.001	<0.001
762	<0.001	<0.001	<0.001	<0.001	<0.001	<0.001	<0.001	<0.001	<0.001
775	<0.001	<0.001	<0.001	<0.001	<0.001	<0.001	<0.001	<0.001	<0.001
786	<0.001	<0.001	0.012	<0.001	<0.001	<0.001	<0.001	<0.001	<0.001
799	<0.001	<0.001	<0.001	<0.001	<0.001	<0.001	<0.001	<0.001	<0.001
811	<0.001	<0.001	<0.001	<0.001	<0.001	<0.001	<0.001	<0.001	<0.001
823	<0.001	<0.001	<0.001	<0.001	<0.001	<0.001	<0.001	<0.001	<0.001
841	<0.001	<0.001	<0.001	<0.001	<0.001	<0.001	0.001	<0.001	<0.001
852	<0.001	<0.001	<0.001	<0.001	<0.001	<0.001	<0.001	<0.001	<0.001
863	<0.001	<0.001	<0.001	<0.001	<0.001	<0.001	<0.001	<0.001	<0.001
872	<0.001	<0.001	<0.001	<0.001	<0.001	<0.001	<0.001	<0.001	<0.001
882	-	<0.001	<0.001	<0.001	<0.001	<0.001	<0.001	<0.001	<0.001
892	<0.001	-	<0.001	<0.001	<0.001	<0.001	<0.001	<0.001	<0.001
901	<0.001	<0.001	-	<0.001	<0.001	<0.001	<0.001	<0.001	<0.001
910	<0.001	<0.001	<0.001	-	<0.001	<0.001	<0.001	<0.001	<0.001
923	<0.001	<0.001	<0.001	<0.001	-	<0.001	<0.001	<0.001	<0.001
930	<0.001	<0.001	<0.001	<0.001	<0.001	-	<0.001	<0.001	<0.001
938	<0.001	<0.001	<0.001	<0.001	<0.001	<0.001	-	<0.001	<0.001
943	<0.001	<0.001	<0.001	<0.001	<0.001	<0.001	<0.001	-	<0.001
954	<0.001	<0.001	<0.001	<0.001	<0.001	<0.001	<0.001	<0.001	-

F

Appendix: Performance of classifiers

Performance linear SVM

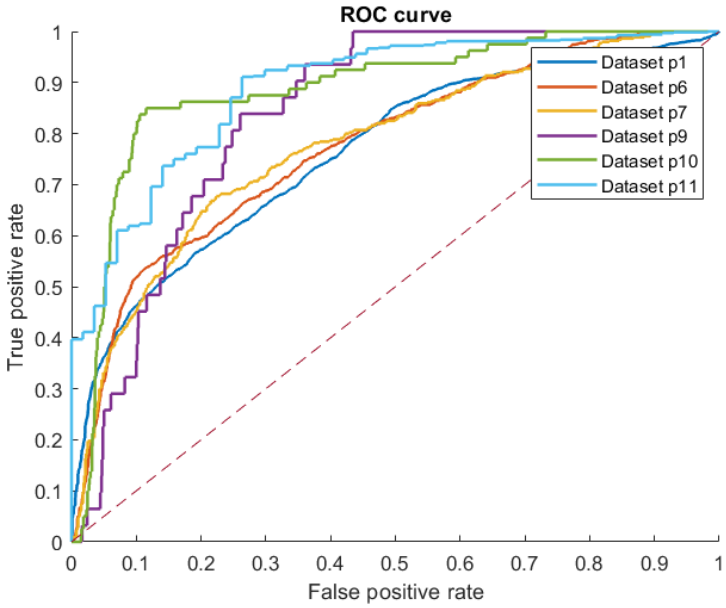

Figure F.1: ROC curve from linear SVM

Table F.1: Performance of linear SVM classification

Patient	TP	FN	FP	TN	Sen	Spec	PPV	NPV	AUC	MCC
1	4616	499	1235	1519	0.911	0.552	0.789	0.772	0.761	0.510
6	561	451	766	5324	0.554	0.874	0.423	0.922	0.792	0.384
7	292	148	164	632	0.664	0.794	0.640	0.810	0.784	0.454
9	29	2	513	1020	0.946	0.665	0.054	0.998	0.844	0.176
10	68	12	158	1144	0.850	0.879	0.301	0.990	0.889	0.460
11	627	61	16	41	0.911	0.719	0.975	0.402	0.893	0.488
Mean					**0.806**	**0.747**	**0.530**	**0.816**	**0.827**	**0.412**

Performance RBF SVM

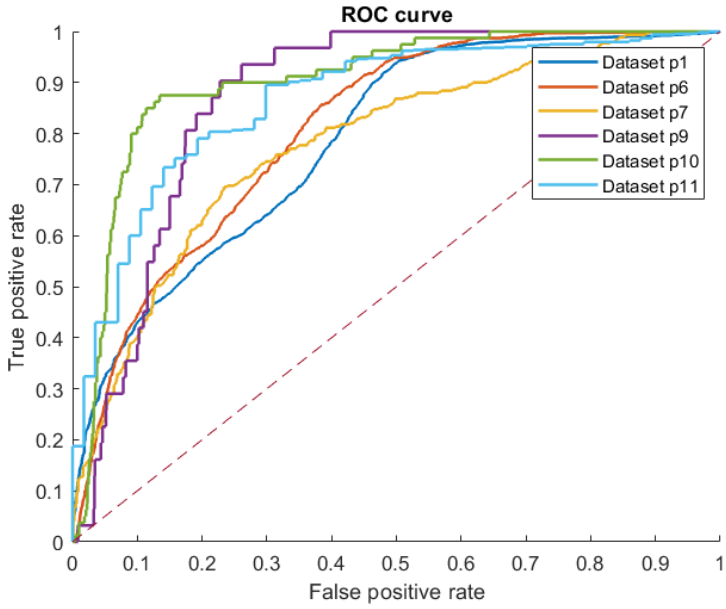

Figure F.2: ROC curve from RBF SVM

Table F.2: Performance of radial basis function SVM classification

Patient	TP	FN	FP	TN	Sen	Spec	PPV	NPV	AUC	MCC
1	4659	406	1323	1431	0.920	0.520	0.779	0.779	0.786	0.495
6	867	145	2334	3756	0.857	0.617	0.271	0.963	0.809	0.333
7	306	134	184	610	0.670	0.766	0.622	0.820	0.781	0.452
9	28	3	349	1184	0.903	0.772	0.074	0.998	0.871	0.220
10	70	10	175	1127	0.875	0.866	0.286	0.991	0.902	0.453
11	544	144	11	46	0.791	0.807	0.980	0.242	0.867	0.364
Mean					**0.836**	**0.725**	**0.502**	**0.799**	**0.836**	**0.386**

Performance k-NN

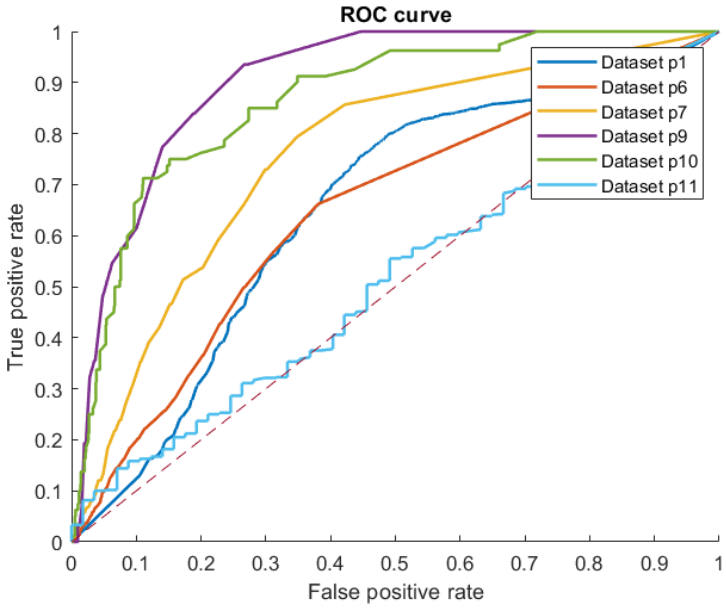

Figure F.3: ROC curve from k-NN classifier

Table F.3: Performance of k-NN classification

Patient	TP	FN	FP	TN	Sen	Spec	PPV	NPV	AUC	MCC
1	4049	1016	1347	1407	0.799	0.511	0.750	0.581	0.649	0.321
6	670	342	2319	3771	0.662	0.619	0.224	0.917	0.647	0.199
7	349	91	277	519	0.793	0.652	0.558	0.851	0.758	0.426
9	29	2	409	1124	0.936	0.733	0.066	0.998	0.903	0.208
10	57	23	144	1158	0.713	0.889	0.284	0.981	0.866	0.399
11	53	589	4	53	0.144	0.930	0.961	0.083	0.514	0.057
Mean					**0.675**	**0.722**	**0.474**	**0.735**	**0.722**	**0.268**

Bibliography

[1] Amnon Amit, Julian Schink, Ari Reiss, and Lior Lowenstein. Pet/ct in gynecologic cancer: present applications and future prospects—a clinician's perspective. PET clinics, 5(4):391–405, 2010.

[2] E. J. M. Baltussen, E. N. D. Kok, S. G. B. de Koning, J. Sanders, A. G. J. Aalbers, N. F. M. Kok, G. L. Beets, C. C. Flohil, S. C. Bruin, K. F. D. Kuhlmann, Hjcm Sterenborg, and T. J. M. Ruers. Hyperspectral imaging for tissue classification, a way toward smart laparoscopic colorectal surgery. J Biomed Opt, 24(1):1–9, 2019. ISSN 1083-3668. doi: 10.1117/1.Jbo.24.1.016002. URL https://www.spiedigitallibrary.org/journals/Journal-of-Biomedical-Optics/volume-24/issue-1/016002/Hyperspectral-imaging-for-tissue-classification-a-way-toward-smart-laparoscopic/10.1117/1.JBO.24.1.016002.pdf.

[3] Elisabeth JM Baltussen, SG Brouwer De Koning, J Sanders, AGJ Aalbers, NFM Kok, Geerard L Beets, BHW Hendriks, Henricus JCM Sterenborg, KFD Kuhlmann, and Theo JM Ruers. Tissue diagnosis during colorectal cancer surgery using optical sensing: an in vivo study. Journal of translational medicine, 17(1): 1–10, 2019.

[4] R. J. Beaulieu, S. D. Goldstein, J. Singh, B. Safar, A. Banerjee, and N. Ahuja. Automated diagnosis of colon cancer using hyperspectral sensing. International Journal of Medical Robotics and Computer Assisted Surgery, 14(3):e1897, 2018. ISSN 1478-5951. doi: 10.1002/rcs.1897. URL https://onlinelibrary.wiley.com/doi/full/10.1002/rcs.1897.

[5] F. Bray, J. Ferlay, I. Soerjomataram, R. L. Siegel, L. A. Torre, and A. Jemal. Global cancer statistics 2018: Globocan estimates of incidence and mortality worldwide for 36 cancers in 185 countries. CA: a cancer journal for clinicians, 68(6):394–424, 2018.

[6] D. E. Cohn, N. C. Hall, S.P. Povoski, L. G. Seamon, W.B. Farrar, and E. W. Martin Jr. Novel perioperative imaging with f-fdg pet/ct and intraoperative f-fdg detection using a handheld gamma probe in recurrent ovarian cancer. Gynecologic oncology, 110(2):152–157, 2008. doi: https://doi.org/10.1016/j.ygyno.2008.04.026.

[7] S. G. B. De Koning, P. Weijtmans, M. B. Karakullukcu, C. Shan, E. J. M. Baltussen, L. A. Smit, R. L. P. van Veen, B. H. W. Hendriks, Hjcm Sterenborg, and T. J. M. Ruers. Toward assessment of resection margins using hyperspectral diffuse reflection imaging (400-1,700 nm) during tongue cancer surgery. Lasers in Surgery and Medicine, 2019. ISSN 0196-8092. doi: 10.1002/lsm.23161. URL https://onlinelibrary.wiley.com/doi/full/10.1002/lsm.23161.

[8] Shahrzad Ehdaivand. Who classification of ovarian neoplasms. Revised, 24, 2013. URL https://www.pathologyoutlines.com/topic/ovarytumorwhoclassif.html.

[9] Himar Fabelo, Martin Halicek, Samuel Ortega, Maysam Shahedi, Adam Szolna, Juan F Piñeiro, Coralia Sosa, Aruma J O'Shanahan, Sara Bisshopp, Carlos Espino, et al. Deep learning-based framework for in vivo identification of glioblastoma tumor using hyperspectral images of human brain. Sensors, 19(4): 920, 2019.

[10] M. Halicek, J. D. Dormer, J. V. Little, A. Y. Chen, L. Myers, B. D. Sumer, and B. W. Fei. Hyperspectral imaging of head and neck squamous cell carcinoma for cancer margin detection in surgical specimens from 102 patients using deep learning. Cancers, 11(9), 2019. ISSN 2072-6694. doi: 10.3390/cancers11091367. URL https://res.mdpi.com/d_attachment/cancers/cancers-11-01367/article_deploy/cancers-11-01367.pdf.

[11] M. Halicek, H. Fabelo, S. Ortega, G. M. Callico, and B. W. Fei. In-vivo and ex-vivo tissue analysis through hyperspectral imaging techniques: Revealing the invisible features of cancer. Cancers, 11(6), 2019. ISSN 2072-6694. doi: 10.3390/cancers11060756. URL https://res.mdpi.com/d_attachment/cancers/cancers-11-00756/article_deploy/cancers-11-00756.pdf.

[12] M. Halicek, H. Fabelo, S. Ortega, J. V. Little, X. Wang, A. Y. Chen, G. M. Callico, L. Myers, B. D. Sumer, and B. W. Fei. Hyperspectral imaging for head and neck cancer detection: specular glare and variance of the tumor margin in surgical specimens. Journal of Medical Imaging, 6(3):035004, 2019. ISSN 2329-4302. doi: 10.1117/1.Jmi.6.3.035004. URL https://www.spiedigitallibrary.org/journals/Journal-of-Medical-Imaging/volume-6/issue-3/035004/Hyperspectral-imaging-for-head-and-neck-cancer-detection--specular/10.1117/1.JMI.6.3.035004.pdf.

[13] M. Halicek, J. V. Little, X. Wang, A. Y. Chen, and B. Fei. Optical biopsy of head and neck cancer using hyperspectral imaging and convolutional neural networks. J Biomed Opt, 24(3):1–9, 2019. ISSN 1083-3668. doi: 10.1117/1.Jbo.24.3.036007.

[14] Benno HW Hendriks, Andrea JR Balthasar, Gerald W Lucassen, Marjolein van der Voort, Manfred Mueller, Vishnu V Pully, Torre M Bydlon, Christian Reich, Arnold TMH van Keersop, Jeroen Kortsmit, et al. Nerve detection with optical spectroscopy for regional anesthesia procedures. Journal of translational medicine, 13(1):1–11, 2015.

[15] C. E. S. Hoogstins, Q. R. J. G. Tummers, K. N. Gaarenstroom, C. D. De Kroon, J. B. M. Z. Trimbos, T. Bosse, V. T. H. B. M. Smit, J. Vuyk, C. J. H. Van De Velde, A. F. Cohen, P. S. Low, J. Burggraaf, and A. L. Vahrmeijer. A novel tumor-specific agent for intraoperative near-infrared fluorescence imaging: A translational study in healthy volunteers and patients with ovarian cancer. Clin Cancer Res, 22(12):2929–2938, 2016. ISSN 1557-3265 1078-0432. doi: 10.1158/1078-0432.Ccr-15-2640. URL http://www.embase.com/search/results?subaction=viewrecord&from=export&id=L610811474https://clincancerres.aacrjournals.org/content/clincanres/22/12/2929.full.pdf.

[16] Ovarian Cancer Information. Ovarian cancer stages, 2020. URL http://www.ovarian-cancer.ie/staging---grade.html.

[17] Steven L Jacques. Optical properties of biological tissues: a review. Physics in Medicine & Biology, 58(11):R37, 2013.

[18] J. V. Jokerst, A. J. Cole, D. Van de Sompel, and S. S. Gambhir. Gold nanorods for ovarian cancer detection with photoacoustic imaging and resection guidance via raman imaging in living mice. ACS Nano, 6(11):10366–10377, 2012. ISSN 1936-086X. URL http://www.embase.com/search/results?subaction=viewrecord&from=export&id=L366405600https://pubs.acs.org/doi/pdf/10.1021/nn304347g.

[19] Ahmareen Khalid and Anwar Ul Haque. Touch impression cytology versus frozen section as intraoperative consultation diagnosis. International Journal of Pathology, pages 63–70, 2018.

[20] E. Kho, B. Dashtbozorg, L. L. De Boer, K. K. Van de Vijver, Hjcm Sterenborg, and T. J. M. Ruers. Broadband hyperspectral imaging for breast tumor detection using spectral and spatial information. Biomedical Optics Express, 10(9):4496–4515, 2019. ISSN 2156-7085. doi: 10.1364/boe.10.004496. URL https://www.ncbi.nlm.nih.gov/pmc/articles/PMC6757478/pdf/boe-10-9-4496.pdf.

[21] E. Kho, L. L. de Boer, K. K. Van de Vijver, F. van Duijnhoven, Mjtfdv Peeters, Hjcm Sterenborg, and T. J. M. Ruers. Hyperspectral imaging for resection margin assessment during cancer surgery. Clinical Cancer Research, 25(12):3572–3580, 2019. ISSN 1078-0432. doi: 10.1158/1078-0432.Ccr-18-2089. URL https://clincancerres.aacrjournals.org/content/25/12/3572.long.

[22] Pieter L Kubben, Karlien J ter Meulen, Olaf EMG Schijns, Mariël P ter Laak-Poort, Jacobus J van Overbeeke, and Henk van Santbrink. Intraoperative mri-guided resection of glioblastoma multiforme: a systematic review. The lancet oncology, 12(11):1062–1070, 2011.

[23] Wei Li, Qian Du, Fan Zhang, and Wei Hu. Collaborative-representation-based nearest neighbor classifier for hyperspectral imagery. IEEE Geoscience and Remote Sensing Letters, 12(2):389–393, 2014.

[24] M. C. Lim, S. S. Seo, S. Kang, S. K. Kim, S. H. Kim, C. W. Yoo, and S. Y. Park. Intraoperative image-guided surgery for ovarian cancer. Quant. imaging med. surg., 2(2):114–117, 2012. ISSN 2223-4292. URL http://ovidsp.ovid.com/ovidweb.cgi?T=JS&CSC=Y&NEWS=N&PAGE=fulltext&D=prem1&AN=23256068https://www.ncbi.nlm.nih.gov/pmc/articles/PMC3508596/pdf/qims-02-02-114.pdf.

[25] Y. Liu, Y. Endo, T. Fujita, H. Ishibashi, T. Nishioka, E. Canbay, Y. Li, S. I. Ogura, and Y. Yonemura. Cytoreductive surgery under aminolevulinic acid-mediated photodynamic diagnosis plus hyperthermic intraperitoneal chemotherapy in patients with peritoneal carcinomatosis from ovarian cancer and primary peritoneal carcinoma: Results of a phase i trial. Ann Surg Oncol, 21(13):4256–4262, 2014. ISSN 1534-4681 1068-9265. doi: 10.1245/s10434-014-3901-5. URL http://www.embase.com/search/results?subaction=viewrecord&from=export&id=L53257033https://www.ncbi.nlm.nih.gov/pmc/articles/PMC4218977/pdf/10434_2014_Article_3901.pdf.

[26] G. L. Lu, J. V. Little, X. Wang, H. Z. Zhang, M. R. Patel, C. C. Griffith, M. W. El-Deiry, A. Y. Chen, and B. W. Fei. Detection of head and neck cancer in surgical specimens using quantitative hyperspectral imaging. Clinical Cancer Research, 23(18):5426–5436, 2017. ISSN 1078-0432. doi: 10.1158/1078-0432.Ccr-17-0906. URL https://clincancerres.aacrjournals.org/content/clincanres/23/18/5426.full.pdf.

[27] M. Maktabi, H. Kohler, M. Ivanova, B. Jansen-Winkeln, J. Takoh, S. Niebisch, S. M. Rabe, T. Neumuth, I. Gockel, and C. Chalopin. Tissue classification of oncologic esophageal resectates based on hyperspectral data. International Journal of Computer Assisted Radiology and Surgery, 14(10):1651–1661, 2019. ISSN 1861-6410. doi: 10.1007/s11548-019-02016-x. URL https://link.springer.com/content/pdf/10.1007%2Fs11548-019-02016-x.pdf.

[28] T. Mangeolle, I. Yakavets, S. Marchal, M. Debayle, T. Pons, L. Bezdetnaya, and F. Marchal. Fluorescent nanoparticles for the guided surgery of ovarian peritoneal carcinomatosis. Nanomaterials, 2018. ISSN 2079-4991. URL http://ovidsp.ovid.com/ovidweb.cgi?T=JS&CSC=Y&NEWS=N&PAGE=fulltext&D=prem2&AN=30050022.

[29] J. N. McAlpine, S. El Hallani, S. F. Lam, S. E. Kalloger, M. Luk, D. G. Huntsman, C. MacAulay, C. B. Gilks, D. M. Miller, and P. M. Lane. Autofluorescence imaging can identify preinvasive or clinically occult lesions in fallopian tube epithelium: A promising step towards screening and early detection. Gynecol Oncol, 120(3):385–392, 2011. ISSN 0090-8258 1095-6859. doi: 10.1016/j.ygyno.2010.12.333. URL http://www.embase.com/search/results?subaction=viewrecord&from=export&id=L51229633https://www.sciencedirect.com/science/article/pii/S0090825810012163.

[30] Nishir Mehta, Shahensha Shaik, Ram Devireddy, and Manas Ranjan Gartia. Single-cell analysis using hyperspectral imaging modalities. Journal of biomechanical engineering, 140(2), 2018.

[31] Ivo Meinhold-Heerlein, Christina Fotopoulou, Philipp Harter, Christian Kurzeder, Alexander Mustea, Pauline Wimberger, Steffen Hauptmann, and Jalid Sehouli. The new who classification of ovarian, fallopian tube, and primary peritoneal cancer and its clinical implications. Archives of gynecology and obstetrics, 293(4):695–700, 2016.

[32] Farid Melgani and Lorenzo Bruzzone. Classification of hyperspectral remote sensing images with support vector machines. IEEE Transactions on geoscience and remote sensing, 42(8):1778–1790, 2004.

[33] Francesca Moro, Stefano Uccella, Antonia Carla Testa, Giovanni Scambia, and Anna Fagotti. Intraoperative ultrasound-guided excision of cardiophrenic lymph nodes in an advanced ovarian cancer patient. International Journal of Gynecologic Cancer, 28(9), 2018.

[34] Sreyankar Nandy, Atahar Mostafa, Patrick D Kumavor, Melinda Sanders, Molly Brewer, and Quing Zhu. Characterizing optical properties and spatial heterogeneity of human ovarian tissue using spatial frequency domain imaging. Journal of biomedical optics, 21(10):101402, 2016.

[35] Dorra Nouri, Yves Lucas, and Sylvie Treuillet. Calibration and test of a hyperspectral imaging prototype for intra-operative surgical assistance. Medical Imaging 2013: Digital Pathology, 8676:86760P, 2013.

[36] Brian Orr and Robert P Edwards. Diagnosis and treatment of ovarian cancer. Hematology/Oncology Clinics, 32(6):943–964, 2018.

[37] A. Oseledchyk, C. Andreou, M. A. Wall, and M. F. Kircher. Folate-targeted surface-enhanced resonance raman scattering nanoprobe ratiometry for detection of microscopic ovarian cancer. ACS Nano, 11(2):1488–1497, 2017. ISSN 1936-0851. URL https://pubs.acs.org/doi/pdf/10.1021/acsnano.6b06796.

[38] S. Palakkan, T. Augestine, M. K. Valsan, K. P. Vahab, and L. K. Nair. Role of frozen section in surgical management of ovarian neoplasm. Gynecology and minimally invasive therapy, 9:13–17, 2020.

[39] C. F. Pop, I. Veys, M. G. Galdon, M. Moreau, D. Larsimont, V. Donckier, P. Bourgeois, and G. Liberale. Ex vivo indocyanine green fluorescence imaging for the detection of lymph node involvement in advanced-stage ovarian cancer. J. Surg. Oncol., 118(7):1163–1169, 2018. ISSN 0022-4790. URL https://onlinelibrary.wiley.com/doi/full/10.1002/jso.25263.

[40] Jaime Prat. Ovarian carcinomas: five distinct diseases with different origins, genetic alterations, and clinicopathological features. Virchows Archiv, 460(3):237–249, 2012.

[41] L. M. Randall, R. M. Wenham, P. S. Low, S. C. Dowdy, and J. L. Tanyi. A phase ii, multicenter, open-label trial of otl38 injection for the intra-operative imaging of folate receptor-alpha positive ovarian cancer. Gynecol Oncol, 155(1):63–68, 2019. ISSN 1095-6859 0090-8258. doi: 10.1016/j.ygyno.2019.07.010. URL http://www.embase.com/search/results?subaction=viewrecord&from=export&id=L2002399419https://www.sciencedirect.com/science/article/abs/pii/S0090825819313964.

[42] Sanathana Konugolu Venkata Sekar, Ilaria Bargigia, Alberto Dalla Mora, Paola Taroni, Alessandro Ruggeri, Alberto Tosi, Antonio Pifferi, and Andrea Farina. Diffuse optical characterization of collagen absorption from 500 to 1700 nm. Journal of biomedical optics, 22(1):015006, 2017.

[43] Bikesh Kumar Singh, Kesari Verma, and AS Thoke. Investigations on impact of feature normalization techniques on classifier's performance in breast tumor classification. International Journal of Computer Applications, 116(19), 2015.

[44] Edward R St John, Merja Rossi, Pamela Pruski, Ara Darzi, and Zoltan Takats. Intraoperative tissue identification by mass spectrometric technologies. TrAC Trends in Analytical Chemistry, 85:2–9, 2016.

[45] Tyler H Tate, Brenda Baggett, Photini FS Rice, Jennifer W Koevary, Gabriel V Orsinger, Ariel C Nymeyer, Weston A Welge, Kathylynn Saboda, Denise J Roe, Kenneth D Hatch, et al. Multispectral fluorescence imaging of human ovarian and fallopian tube tissue for early-stage cancer detection. Journal of biomedical optics, 21(5):056005, 2016.

[46] Q. R. J. G. Tummers, C. E. S. Hoogstins, A. A. W. Peters, C. D. De Kroon, J. B. M. Z. Trimbos, C. J. H. Van De Velde, J. V. Frangioni, A. L. Vahrmeijer, and K. N. Gaarenstroom. The value of intraoperative near-infrared fluorescence imaging based on enhanced permeability and retention of indocyanine green: Feasibility and false-positives in ovarian cancer. PLoS ONE, 10(6), 2015. ISSN 1932-6203. doi: 10.1371/journal.pone.0129766. URL http://www.embase.com/search/results?subaction=viewrecord&from=export&id=L605398337https://journals.plos.org/plosone/article/file?id=10.1371/journal.pone.0129766&type=printable.

[47] G. M. Van Dam, G. Themelis, L. M. A. Crane, N. J. Harlaar, R. G. Pleijhuis, W. Kelder, A. Sarantopoulos, J. S. De Jong, H. J. G. Arts, A. G. J. Van Der Zee, J. Bart, P. S. Low, and V. Ntziachristos. Intraoperative tumor-specific fluorescence imaging in ovarian cancer by folate receptor-α targeting: First in-human results. Nat Med, 17(10):1315–1319, 2011. ISSN 1078-8956 1546-170X. doi: 10.1038/nm.2472. URL http://www.embase.com/search/results?subaction=viewrecord&from=export&id=L51625420https://www.nature.com/articles/nm.2472.

[48] I. Veys, F. C. Pop, S. Vankerckhove, R. Barbieux, M. Chintinne, M. Moreau, J. M. Nogaret, D. Larsimont, V. Donckier, P. Bourgeois, and G. Liberale. Icg-fluorescence imaging for detection of peritoneal metastases and residual tumoral scars in locally advanced ovarian cancer: A pilot study. J Surg Oncol, 117(2):228–235, 2018. ISSN 1096-9098 0022-4790. doi: 10.1002/jso.24807. URL http://www.embase.com/search/results?subaction=viewrecord&from=export&id=L620891863https://onlinelibrary.wiley.com/doi/full/10.1002/jso.24807.

[49] P. Wang, Y. Fan, L. Lu, L. Liu, L. Fan, M. Zhao, Y. Xie, C. Xu, and F. Zhang. Nir-ii nanoprobes in-vivo assembly to improve image-guided surgery for metastatic ovarian cancer. Nat Commun, 9(1), 2018. ISSN 2041-1723. doi: 10.1038/s41467-018-05113-8. URL http://www.embase.com/search/results?subaction=viewrecord&from=export&id=L623176581https://www.nature.com/articles/s41467-018-05113-8.pdf.

[50] A. A. Wright, K. Bohlke, D. K. Armstrong, M. A. Bookman, W. A. Cliby, R. L. Coleman, D. S. Dizon, J. J. Kash, L. A. Meyer, K. N. Moore, A. B. Olawaiye, J. Oldham, R. Salani, D. Sparacio, W. P. Tew, I. Vergote, and M. I. Edelson. Neoadjuvant chemotherapy for newly diagnosed, advanced ovarian cancer: Society of gynecologic oncology and american society of clinical oncology clinical practice guideline. Gynecol Oncol, 143(1):3–15, 2016. ISSN 1095-6859 0090-8258. doi: 10.1016/j.ygyno.2016.05.022. URL http://www.embase.com/search/results?subaction=viewrecord&from=export&id=L612620213.

[51] Y. Yonemura, E. Canbay, H. Ishibashi, E. Nishino, Y. Endou, S. Sako, and S. I. Ogura. 5-aminolevulinic acid fluorescence in detection of peritoneal metastases. Asian Pac J Cancer Prev, 17(4):2271–2275, 2016. ISSN 2476-762X. URL http://www.embase.com/search/results?subaction=viewrecord&from=export&id=L614863015.